TAMPEREEN TEKNILLINEN YLIOPISTO
TAMPERE UNIVERSITY OF TECHNOLOGY

Juha Hirvonen

Computer Vision Measurements for Automated Microrobotic Paper Fiber Studies

Julkaisu 1456 • Publication 1456

Tampere 2017

Tampereen teknillinen yliopisto. Julkaisu 1456
Tampere University of Technology. Publication 1456

Juha Hirvonen

Computer Vision Measurements for Automated Microrobotic Paper Fiber Studies

Thesis for the degree of Doctor of Science in Technology to be presented with due permission for public examination and criticism in Festia Building, Auditorium Pieni Sali 1, at Tampere University of Technology, on the 10th of February 2017, at 12 noon.

Tampereen teknillinen yliopisto - Tampere University of Technology
Tampere 2017

ISBN 978-952-15-3904-6 (printed)
ISBN 978-952-15-3906-0 (PDF)
ISSN 1459-2045

Abstract

The mechanical characterization of paper fibers and paper fiber bonds determines the key parameters affecting the mechanical properties of paper. Although bulk measurements from test sheets can give average values, they do not yield any real fiber-level data. The current, state-of-the-art methods for fiber-level measurements are slow and laborious, requiring delicate manual handling of microscopic samples. There are commercial microrobotic actuators that allow automated or tele-operated manipulation of microscopic objects such as fibers, but it is challenging to acquire the data needed to guide such demanding manipulation. This thesis presents a solution to the illumination problem and computer vision algorithms for obtaining the required data. The solutions are designed for a microrobotic platform that comprises actuators for manipulating the fibers and one or two microscope cameras for visual feedback.

The algorithms have been developed both for wet fibers, which can be treated as 2D objects, and for dry fibers and fiber bonds, which are treated as 3D objects. The major innovations in the algorithms are the rules for the micromanipulation of the curly fiber strands and the automated 3D measurements of microscale objects with random geometries. The solutions are validated by imaging and manipulation experiments with wet and dry paper fibers and dry paper fiber bonds. In the imaging experiments, the results are compared with the reference data obtained either from an experienced human or another imaging device. The results show that these solutions provide morphological data about the fibers which is accurate and precise enough to enable automated fiber manipulation. Although this thesis is focused on the manipulation of paper fibers and paper fiber bonds, both the illumination solution and the computer vision algorithms are applicable to other types of fibrous materials.

Preface

“First of all, I would thank myself. Then, the jury.” With these words director Aki Kaurismäki accepted the Grand Prix award in Cannes film festival in 2002.

My jury consists of Prof. Sergej Fatikow from Carl von Ossietzky University of Oldenburg, Prof. Jarmo Alander from University of Vaasa, and Assoc. Prof. Ulrich Hirn from Graz University of Technology. I am grateful for Prof. Fatikow and Assoc. Prof. Hirn for their efforts in pre-examining my dissertation and giving valuable feedback. I would also like to thank Prof. Fatikow and Prof. Alander for accepting the request to be my opponents.

As I have a reputation for being far more talkative than Mr. Kaurismäki, I’ll still continue.

Prof. Pasi Kallio did a great job in being the director of this film and I would like to express my deepest gratitude for his guidance during the long and not-always-so-smooth creative process. I entered his lab as a summer worker in 2005, did my master’s thesis there in 2010, and now is the time for the final installment of the saga. Thanks for the micro years!

I acknowledge my executive producer GETA graduate school and the co-executive producers Academy of Finland and Tekes for funding. Special thanks belong to Prof. Ari Sihvola and Ms. Marja Leppäharju – the director and the coordinator of GETA – for organizing interesting intensive courses and enjoyable social activities.

I appreciate the whole film crew MST-group for providing a pleasant environment for the production. I would like to thank especially the fiber team, namely MSc Mathias von Essen for the special effects, PhD Pooya Saketi and MSc Kourosh Latifi for the set design and MSc Yuli Lai for the stunts.

I am truly grateful for my support team: my father Tuomo, my mother Anja and my brother Vesa for always being there for me, in joys and hardships. Also, my friends deserve the warmest hugs for the great and fiberless free time we have had together.

Last but not least, I’ll bow down before the actress in a leading role Maiju for her love and support, which kept me moderately sane during the painful creation of the script.

Helsinki 9.1. 2017

Juha Hirvonen

Contents

List of Symbols and Abbreviations

µCT	X-ray microtomography
AFM	Atomic-force microscopy
CAD	Computer-aided design
CCD	Charge-coupled device
DLT	Direct linear transformation
ESEM	Environmental scanning electron microscopy
FEM	Finite element method
FFIF	Finnish Forest Industries Federation
FLER2	Fiber load elongation recorder
ICP	Iterative closest point
PDMS	Polydimethylsiloxane
SEM	Scanning electron microscopy

α	Rotation angle about Z axis
β	Rotation angle about Y axis
γ	Rotation angle about X axis
δ_u, δ_v	Focal length multiplied by the horizontal and the vertical transformation factor
η_x, η_y	Pixel-to-metric coefficient in the X and the Y direction
θ_{ij}	Angles in the three grasping sections of a bond, i = 1…3, j = 1,2
θ_{max}	Maximum angle in the grasping section of a bond
θ_{min}	Minimum complementary angle in the grasping section of a fiber
ξ	Zoom factor
$b(u, v)$	Binary image

$C(p)$	Number of distinct 8-connected components in the 3 x 3 neighborhood of pixel p
d	Small gap between the focal plane and the object plane
$\bar{d}$	Distance between the microscope objective and the sample
d_a	Distance between the grasp point and the adjacent fiber
d_e	Distance between the grasp point and the fiber end point
d_p	Distance between a primary point and the bonding point
d_s	Distance between the secondary point and the bonding point
e_1, e_2	Ending lengths of a fiber
e_{min}, e_{max}	Minimum and maximum ending lengths of a fiber
f	Focal length
f_{ob}	Focal length of the microscope lens
f_{TL}	Microscope tube length
$f(u, v)$	Grayscale image
$\mathbf{K}$	Calibration matrix
K	Intermediate skeleton image used in pruning
k_1, k_2	Coefficients of radial distortion
$\mathbf{L}$	Similarity transformation for normalizing 3D points for DLT
L'	Length of the fiber section between the grasp points of a fiber
l_{min}	Minimum length of the fiber section between the grasp points of a fiber
$\mathbf{M}$	Cartesian 3D coordinate, a 3-vector
$\tilde{\mathbf{M}}$	Homogeneous Cartesian 3D coordinate, a 4-vector
$\mathbf{m}$	Cartesian 2D coordinate, a 2-vector
$\tilde{\mathbf{m}}$	Homogeneous Cartesian 2D coordinate, a 3-vector
m_x , m_y	Transformation factors from the world coordinates to the pixel coordinates in the x and y direction

N_p	Pixel threshold in pruning
P	Camera matrix
$\mathbf{p}^i$	*i*th row of **P**, $i = 1…3$
p_i	Pixel in the 3 x 3 neighborhood of pixel p, $i = 1…8$
p_x, p_y	x and y coordinate of the principal point
R	Rotation matrix
r_{ij}	Terms of the rotation matrix, $i = 1…3$, $j = 1…3$
r	Distance from the center of the radial distortion
S	Second result matrix of the SVD of a m x n matrix, a diagonal m x n matrix
S	Skeleton image
s	Skew factor
T	Similarity transformation for normalizing image points for DLT
t	Translation vector
t_x, t_y, t_z	Translations in X, Y and Z direction
U	First result matrix of the SVD of a m x n matrix, a m x m unitary matrix
u, v	Horizontal and vertical image coordinates
u'', v''	Distorted horizontal and vertical image coordinates
u_0 ,v_0	Horizontal and vertical image coordinate of the principal point
V	Third result matrix of the SVD of a m x n matrix, a n x n unitary matrix
W	Scale in the homogeneous Cartesian 3D coordinate
w	Scale in the homogeneous Cartesian 2D coordinate
X, Y, Z	Cartesian 3D coordinates
x, y	Cartesian 2D coordinates

List of Publications

I. Hirvonen, J., Hänninen, A. & Kallio, P. Design and implementation of an illumination system for microrobotic paper fiber studies, Proceedings of IEEE/RAS International Conference on Robotics and Automation (ICRA 2014), 31.5. – 7.6.2014, Hong Kong, China, pp. 5854 – 5859.

II. Hirvonen, J. & Kallio, P. 2015 Automatic image-based detection and inspection of paper fibres for grasping, IET Computer Vision, vol. 9, no 4, pp. 588 – 594.

III. Hirvonen, J. & Kallio, P. Scale and rotation invariant microgripper detection that uses a planar pattern in a microrobotic two view system. Proceedings of IFAC Symposium on Mechatronic Systems (Mechatronics '13), 10. – 12.4.2013. Hangzhou, China, pp. 414 – 422.

IV. Hirvonen, J., Myllys, M. & Kallio P. 2016. Method for 3D fibre reconstruction on a microrobotic platform, Journal of Microscopy, vol. 263, no 1, pp. 20 – 33.

V. Hirvonen, J., Essen, M. von & Kallio, P. Automated microrobotic manipulation of paper fiber bonds, Proceedings of IEEE/RSJ International Conference on Intelligent Robots and Systems (IROS 2015), 28.9. – 8.10.2015, Hamburg, Germany, pp. 784 – 789.

1 Introduction

1.1 Motivation

In this exciting and rapidly changing era of digitalization, the forestry industry is still a major player in the Finnish economy and is one of the country's largest employers. Forestry products accounted for 20% of Finland's exports in 2015 (Finnish customs) and the value of the paper and board exported was almost 7 billion euros (Finnish Forest Industries Federation, (FFIF) 2016).

It is the fibers that are the major structural element of paper, and separating these fibres, whether they come from wood, fiber crops or waste paper, can be done either mechanically or chemically. Paper fibers are typically a couple of millimeters long and some tens of micrometers wide, depending on their source. A single sheet of paper consists of a network of millions of paper fibers bonded together. It is therefore clear that the physical and chemical properties of these fibers will define the physical and chemical properties of the paper (Sirviö 2008), and it follows that being able to measure these properties quickly and reliably is of great interest to the research community in the pulp and paper industry.

Conventionally, the physical properties of pulp are defined using specially manufactured circular hand sheets (TAPPI Quality and Standards Department 2001). However, although the measurements obtained with these devices can give average values, they cannot give any real fiber-level data. Since paper fibers are natural objects, they are highly heterogeneous, and being able to define the distribution of their physical properties would provide much more useful information than can be gained from an average value. Indeed, the distribution of these physical properties also defines the degree of confidence that can be placed in any average value.

Fiber-level measurements have been done since the 1950s, and although the measuring devices have advanced dramatically, there has not been much development in the technology for handling the fibers. Obtaining the distribution of the fibers is not an easy task. It requires a great number of measurements from individual paper fibers and paper fiber bonds. Current best practice is that the paper fibers and paper fiber bonds are still attached to the measurement system manually, which is

a time-consuming and laborious task. Therefore, the number of measurements that can be taken over a given period is so low that they have no statistical relevance. There is clearly a need for an automated system capable of making rapid, high-throughput measurements.

Recent advances in microsystems, and in particular, microrobotics, have enabled rapid progress to be made in the relatively new field of microassembly (Probst et al. 2009; Das et al. 2012) and in the automated manipulation of nanomaterials (Eichhorn et al. 2007; Bartenwerfer et al. 2013), biomaterials (Kim et al. 2008; Hirvonen et al. 2008), living cells (Matsuoka et al. 2005; Wang et al. 2007; Kovanen et al. 2007) and sub-cellular components (Sun et al. 2005). It should therefore come as no surprise that microrobotic tools have now entered the domain of paper fiber research. Versatile and flexible platforms have been developed that have greatly facilitated the processes for handling and measuring paper fibers and paper fiber bonds (Saketi et al. 2010; Saketi & Kallio 2011b; Mikczinski et al. 2013). However, these systems are not highly automated as most of the research in the field has concentrated on mapping possible applications and performing proof-of-concept type of experiments. With the current technology, an experienced user is always needed to control the platform in tele-operated mode, and although the execution time for the procedure is better than it would have been if it were done manually, the yield has still remained low (Saketi et al. 2012). Nevertheless, the results gained from these experiments show the potential benefits of using automated microrobotic platforms for handling and measuring paper fibers.

The current challenge to automating the functions of a microrobotic platform to handle paper fibers is the need for new methods of acquiring information about the target fibers, as this data is needed in order to accurately guide the manipulators of the automated platform in their tasks. The only reasonable technique for this is computer vision. The purpose of this thesis is to create imaging solutions and computer vision algorithms that can be used to enable automated fiber manipulation on a microrobotic platform.

1.2 Research Questions

The computer vision algorithms used should be capable of detecting paper fibers or paper fiber bonds placed on a platform, and then deciding whether they are graspable with the actuators on the platform. Such an inspection will require exact knowledge of the geometry of the targets. These algorithms also need to be able to define the grasp points, i.e. the most suitable points at which the fibers should be grasped by the automated mechanism. Therefore, the main research questions in this thesis can be summarized as follows:

- Can the imaging of paper fibers and paper fiber bonds be improved to such a level that they can be detected and defined individually with minimal computation, thus enabling the possibility of their efficient automated manipulation?
- What information should be gathered from the images of thin, curly and irregular planar objects that wet paper fibers are that would enable the possibility of their automated microrobotic manipulation?
- How can a microrobotic platform, consisting of the microscope cameras and microgripper actuators required for image-based 3D measurements and grasping experiments, be accurately calibrated?
- How to perform 3D measurements on the thin, curly, highly heterogenous non-planar objects which dry paper fibers are, in order to gain enough information about their depth to enable their automated manipulation?
- Is it possible to define suitable grasp points for these thin, curly and irregular objects so that they can be grasped and manipulated by microgripper actuators in an automated manner?

1.3 Contributions

This thesis presents hardware and software solutions for various studies of automated paper fiber handling. The main contributions of the thesis are the following:

- A polarized backlight -based illumination system that produces high-contrast images of the paper fibers and paper fiber bonds for microhandling/manipulation purposes
- A graspability inspection and grasp point detection algorithm for wet paper fibers that can be treated as 2D objects (grasp point detection is extendable for 3D fibers as well)
- A 3D calibration and gripper tracking method for the microrobotic platform with two cameras
- A 3D reconstruction algorithm for dry paper fibers and dry paper fiber bonds, both as 3D objects
- A grasp point detection algorithm for dry paper-fiber bonds

The contributions are presented in the following five publications. The main points of the publications are described below.

Publication I discusses the design and implementation of the illumination system. It describes the experiments performed to compare different illumination schemes, and the implementation of the final optimal system using polarized light. The novelty of the paper lies in the integration of a polarized light source in the micromanipulation test bench. The designed illumination system is used in Publications II, IV and V. The functioning of the final illumination system is validated at the end of the work. The author planned the tests, conceived the design, analyzed the data and wrote the article.

Publication II describes an algorithm for detecting individual paper fibers from a microscope image, inspecting them to see if they are graspable and calculating suitable grasp points. In these experiments, the fibers were wet and stayed planar. The results of the algorithm were compared with the results of an experienced human user and the analysis of the results is presented. The innovation described in this article was the generation of morphology-based rules for grasping individual fibers with microgrippers. The author wrote the algorithm, designed and performed the experiments, analyzed the data and wrote the article.

Publication III discusses calibrating the microrobotic platform, which consists of two cameras and microgripper actuators, in such a way that it can take 3D measurements. This article descibes how the gripper actuator can be detected from the images regardless of its orientation. An inexpensive and easily fabricated marker was made and attached to the gripper. The novelty of the paper was that it presented the calibration of a 3D microrobot and microscope camera setup that does not use template matching, does not require micromanufacturing methods for the marker and does not depend on the scale and the orientation of the actuator tool. The author wrote the algorithms, designed and performed the experiments, analyzed the data and wrote the paper.

Publication IV presents an algorithm for reconstructing the 3D geometry of dry paper fibers from two images taken from different views. The reconstructed 3D geometries were compared with the references produced with X-ray microtomography (µCT). Four paper fibers are imaged in 16 different orientations in the experiments. The novelty in this paper was that it provided 3D reconstructions of fibrous objects on a microrobotic platform and compared these with the references. The author gratefully acknowledges the work of Markko Myllys for his contribution to the µCT part; the rest of the article is the author's own work.

Publication V describes an algorithm for deciding whether or not a bond formed by two paper fibers is graspable, and then calculating its grasp points. The algorithm illustrated in Publication III is developed to encompass the 3D geometry of a paper fiber bond and its geometry is inspected as described in Publication II. The algorithm was used in automated manipulation experiments on seven paper fiber bonds. The novelty of this paper was that it generated rules to enable the automated grasping of individual fiber bonds, and demonstrated that the automated grasping of these fibres was possible. The author wrote the algorithm for this procedure, and most of the article.

1.4 Outline of the Thesis

The thesis consists of five chapters, including this one. Chapter 2 discusses the background to the research and describes the structure and production of paper fibers and paper fiber bonds. The motivation for fiber-level testing is explained and the different methods of testing the physical

properties of paper fibers and the paper fiber bonds presented in the literature are described, as are their major drawbacks. This chapter also presents state-of-the-art automated microrobotic grasping mechanisms and the latest computer vision techniques for imaging different fibers, and these are the methods used to manipulate the paper fibers and paper fiber bonds as described in this thesis. Chapter 2 also discusses the drawbacks of the current state-of-the-art automated manipulators for paper fibers and paper fiber bonds, and how they need to be improved.

Chapter 3 gives a detailed description of the microrobotic platforms used in the experiments for.this thesis. It also deals with how the different paper fiber and paper fiber bond samples were prepared for the experiments. The chapter also describes the methodology for performing metric measurements from images and discusses the camera models, camera calibration techniques and the 3D reconstruction method.

Chapter 4 describes the experiments performed for each of the five published articles that form the basis of this work, and discusses the results obtained from all of these experiments. The chapter first discusses the experiments performed for detecting paper fibers and paper fiber bonds from the image. This is followed by a brief description of the tests done for wet fiber detection and inspection. The next three sections discuss all the experiments needed for the 3D reconstruction, i.e.camera calibration, the 3D reconstruction of dry paper fibers and the 3D reconstruction of paper fiber bonds. They are followed by a description of the studies on grasp point detection. The chapter concludes with a section discussing the performance of the developed methodology.

Chapter 5 states the main conclusions that can be drawn from this thesis and points out the next steps that need to be taken in order to make automated paper fibre handling and measuring a reality.

2 Background and State-of-the-art

This chapter presents the background of the thesis and discusses the state-of-the-art methods for fiber testing, fiber imaging and automated microrobotic grasping. Section 2.1 describes the making and the properties of paper fibers and paper fiber bonds, and Section 2.2 discusses different methodologies for testing the structural properties of individual paper fibers and paper fibers bonds. Section 2.3 introduces the novel methodologies suitable for individual fiber testing and discusses the challenges that have prevented their use in this application this far.

2.1 Paper Fibers and Paper Fiber Bonds

2.1.1 Paper Fibers

Macroscopically, the trunk of a tree has two sections, bark and wood. The bark is the outermost layer of the tree and its function is to protect the tree. Wood is the core of the tree and it is responsible of transport of water and nutrients in the tree. Wood consists primarily of cellulose, hemicellulose and lignin, and it is built of tubular cells that are bound to each other with extra-cellular matrix, the middle lamella. The wood cells are also called as wood fibers and they comprise a two-part cell wall and a hollow lumen. The thin outermost part of the wall is termed the primary wall and it consists primarily of lignin. The thick innermost secondary wall is commonly further divided into three layers: S_1, S_2 and S_3. The majority of the cellulose is distributed in the secondary wall. (Willför et al. 2011). The cellulosic wood fiber cores have the affinity to bond to each other when dried from water or some other polar liquid (Sirviö 2008). This tendency is the foundation of papermaking. Figure 1 shows the structure of wood and wood fiber.

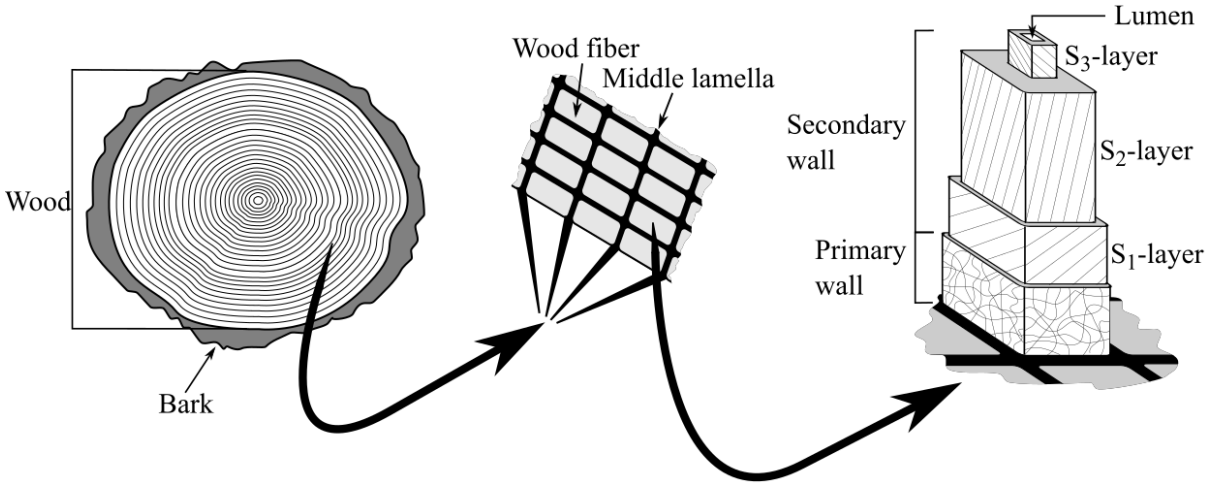

***Figure 1**. The structure of wood and wood fiber. Adapted from (Biermann 1996, p. 14; Sirviö 2008, p. 63).*

The cellulosic wood fiber cores have to be separated from the other components of wood in order to produce paper. This process is called as pulping and there are two main strategies: mechanical or chemical pulping (Biermann 1996, pp. 55-100; Sirviö 2008). In addition to the middle lamella, the primary wall and the S_1 layer are commonly removed in pulping (Sirviö 2008). Remaining fibers are commonly called as pulp fibers, papermaking fibers or paper fibers. In this thesis, the name 'paper fiber' is used. Often, only 'fiber' is used if there is no risk of confusion.

Mechanical pulping refers to the methods where the wood is broken down fully mechanically by grinding or refining (Biermann 1996, pp. 55-100; Sirviö 2008; Sundholm & Lönnberg 2009). In grinding, the wood logs are pressed against a revolving grindstone whereas a rotating disc is used in refining (Sundholm & Lönnberg 2009). The lignin and hemicellulose have to be softened with hot water in order to remove them in the process (Sundholm & Lönnberg 2009). Resulting fibers are thin, thick and straight, and the lignin content of the pulp is high (Biermann 1996, pp. 55-100; Sirviö 2008).

Chemical pulping uses chemicals to dissolve lignin and thus disintegrate wood into fibers (Gustafsson et al. 2011). The most dominant technique is kraft pulping, which utilizes sodium hydroxide and sodium sulfide as the main chemicals (Gustafsson et al. 2011). The fibers produced with chemical pulping are longer, thinner and stronger, and the lignin content is lower compared with mechanical pulping (Biermann 1996, pp. 55-100; Sirviö 2008).

In addition to the pulping method, the fiber dimensions depend also naturally on the type of the wood used in pulping. The fibers are longer and wider in softwoods such as pine and spruce and shorter and thinner in hardwoods such as birch and eucalyptus (Sirviö 2008). The length and width ranges

of common softwoods are 2.8 – 7.0 mm and 27 – 65 µm, respectively, and the corresponding values of typical hardwoods are 0.8 – 1.3 mm and 14 – 28 µm (Sirviö 2008).

Commonly, the pulp is bleached to increase its brightness. This is based on removal of the residual lignin in the case of chemical pulp, and on destruction of some of the colored lignin groups in the case of mechanical pulp, whose lignin content is remarkably higher (Lindholm et al. 2009).

The different fibers produced due to a different wood type or a different pulping technique have also different applications. Newsprint uses primarily mechanical pulp whereas chemical pulp is mostly utilized in manufacturing printing paper (Sirviö 2008).

It is worth to mention that apart from wood, certain crops such as bamboo, rice and wheat are important raw materials for paper in some parts of the world, and they are used in specialty papers worldwide (Sirviö 2008). Also, a bigger and bigger portion of paper is made of recycled fibers. 71% of the paper and paperboard in Finland and about 50% of the paper and paperboard in Europe was recycled in 2012 (FFIF 2013). When the fibers are acquired from the waste paper, removing the non-usable compounds with steps such as slushing, cleaning and de-inking is required (Biermann 1996, p. 266). These processes change the fiber properties such as morphology, flexibility and bonding capability, which limits the recyclability and continues the need for pulp production (Ackermann et al. 2009).

2.1.2 Paper Fiber Bonds

Paper fibers bond to each other when they are dried from water or other polar liquid. This is utilized in papermaking where the wet pulp is pressed and dried to form paper. Depending on the characterization, four (Sirviö 2008), five (Lindström et al. 2005) or six (Hirn & Schennach 2015) bonding mechanisms have been reported in the literature. Nevertheless, the commonly adopted principle is that the surface tension forces drag the fibers closer to each other and then chemical and molecular reactions such as hydrogen bonding and van der Waals interactions bond the fibers together (Sirviö 2008; Lindström et al. 2005). Hydrogen bonding was regarded the most important factor for long (Sirviö 2008) but recent studies prove that van der Waals interactions are more significant (Hirn & Schennach 2015). Paper sheet is a network consisting of fibers and bonds that connect the fibers together.

2.2 Fiber-level Testing

As the single fibers and bonds are the building blocks of paper, their properties affect greatly the properties of paper. Although paper is a network and therefore cannot be thought as a mere group

of inert fibers and bonds, the network structure is dependent on the properties of its building blocks (Sirviö 2008).

The properties such as strength, thickness and light-scattering coefficient of pulp are commonly defined by utilizing special hand sheets and specific testing equipment such as a tensile tester. The production and the dimensions of the hand sheets as well as the test protocols are well-standardized (TAPPI Quality and Standards Department 2002; TAPPI Quality and Standards Department 2001). The tests utilizing the hand sheets help in understanding the properties of the paper made from the type of the pulp in use. However, these tests cannot give direct information of the fiber-level properties since the properties of the network affect the results. Also, the properties of the fiber segments and the properties of the bonds cannot be separated from the measurement data (Sirviö 2008). Understanding how the development of fibers and bonding can help in improving the paper quality requires measurement data from the individual fibers and bonds (Heikkurinen 1999). The data are then applied in mathematical models and statistical analysis (Heikkurinen 1999; Kulachenko et al. 2007; Torgnysdotter et al. 2007; Kulachenko & Uesaka 2012).

2.2.1 Mechanical Testing of Individual Fibers

Fiber properties have an effect on the formation and consolidation of the paper structure in papermaking, and they are also responsible for the properties of the ready paper (Sirviö 2008). Measurements on wet fibers produce data that is relevant for the papermaking process and measurements on dry fibers provide parameters that describe the end product. Measurements on wet fibers are also important for studying the properties of never-dried fibers – pulp that is stored with high water content instead of being dried (Seth 2001; Wang 2006). Online-compatible optical methods for measuring wet fiber dimensions such as length, width and fiber wall thickness have been developed. There are several commercial devices designed for this (Hirn & Bauer 2006). However, measurements of the mechanical properties such as flexibility and strength of individual fibers are far less mature. There has been only one commercial online-compatible device which can deliver fiber flexibility (Hirn & Bauer 2006; Rusu et al. 2011). Otherwise, the measurements of the mechanical properties have to be done in the laboratory conditions.

Fiber flexibility is the inverse of fiber bending stiffness. It is claimed to be one of the most important fiber properties (Lowe 2007). Wet fiber flexibility affects the sheet density, the number of the bonds formed, the area of the bonds (Eckhart et al. 2009), the drainage (Helle 1978) and the wet web strength (Meindersma et al. 1961). Dry fiber flexibility influences the tensile strength, the surface smoothness and the porosity of paper sheets (Paavilainen 1993). Methods to measure the single fiber flexibility or bending stiffness include bending beam methods and classification methods. In the bending beam methods, the deflection of the fiber due to a known force is observed, and the flexibility is calculated using the deflection, the force and the fiber dimensions (Eckhart et al. 2009). Schniewind et al. (1966) fixed the fiber from its one end and applied force to the free end with a small

quartz spring. The deformation of the spring and the deflection of the fiber were determined from the microscope image and the fiber bending stiffness was calculated utilizing those values. Wet and dry fibers were measured with the system. One of the best-known bending beam methods for single fiber flexibility is the one by Tam Doo and Kerekes (1981). They attached the fiber from its ends to a V-shaped notch in the end of a thin tube. The water flow inside the tube caused a hydrodynamic force that deflected the fiber. The deflection was observed visually with a microscope. Olson et al. (1995) tackled the need for fixing the fiber by using a T-junction structure where a capillary fed the fibers in suspension into a perpendicular main channel where liquid was flowing. The flow deflected the fibers after they entered to the main channel, and the deflection was recorded by a CCD camera. The methods by Tam Doo and Kerekes (1981) and Olson et al. (1995) are usable only for wet fibers. Saketi et al. (2010) were the first ones to use microrobotics in the flexibility measurement. The fibers were placed on a rotary stage of the microrobotic platform. There was a small layer of water on the stage to keep the fibers moist. Then, the fibers were grasped from their both ends with two microgrippers, lifted up, pulled straight and pushed with a microsensor tip. The caused deflection was obtained from the position sensor of the actuator that moved the force sensor, the used force from the force sensor and the fiber length from the CCD camera. The method can be used with wet and dry fibers. The classification method for measuring the fiber flexibility utilizes fiber motion in a laminar flow with shear forces. Meindersma et al. (1961) used high-viscosity liquid and two concentric cylinders as the source of the shear force. The fiber was placed into the liquid and the rotations and the translations it exhibited were observed with a microscope. Then, the flexibility was determined from the observed rotations and translations. Eckhart et al. (2009) used a cross-shaped channel structure, where two streams with identical flow rate but opposite directions were meeting in the crossing and discharging to the two intersecting channels. The fibers were diluted in the other of the inlet flows and they were transformed in the crossing. A high-speed camera captured images of the individual fibers in the crossing, and the deformation was compared with a simulation of an ideally flexible fiber with identical dimensions. Flexibility is here defined as the ratio between the deformation of the real fiber and the deformation of the ideal fiber. Thus, the result is a dimensionless flexibility parameter. Both of the classification methods described are usable only to the wet fibers. Lorbach et al. (2014) used a measurement method, which differed completely from the bending beam and classification methods described. They defined the elastic modulus of the fiber with a tensile tester, and then sliced the fiber with an automated microtome for determining the moment of inertia. Then, the fiber bending stiffness was calculated from those values. They measured wet and dry fibers with the method.

Measuring the fiber strength yields the axial tensile strength of the fiber. Material properties such as elastic modulus and stretch at break can be calculated when the stress – strain curve of the individual fibers is known (Heikkurinen 1999). The fiber strength is measured with a tensile tester, to which the fiber is attached from its both ends. The first measurements date back to the turn of 1950s and 1960s (Jayne 1959; Leopold & McIntosh 1961). Later, an imaging device has been added to the test bench in order to obtain more information from the relation of the microstructure to the strength. Page et al.

(1977) used a modified tensile tester in the tensile strength measurement, and a video camera in detecting the effect of natural and process induced defects on the strength of the individual fibers. Micromechanical deformations close to the defect areas during the tensile strain have also been studied using similar equipment and environmental scanning electron microscopy (ESEM) by Mott (1995) and with a confocal scanning microscope by Hamad and Provan (1995). The tensile tests could be done with a similar arrangement as used by Saketi if the grippers were strong enough and the force sensor was integrated in one of the grippers.

2.2.2 Mechanical Testing of Individual Fiber Bonds

Individual fiber bonds have been fabricated for testing purposes by pressing two moist fibers against each other and letting them dry so that a bond forms between them. Right angle between the fibers is desirable but often hard to achieve (Saketi 2015). Bond strength is measured by pulling the fibers apart from each other and measuring the force needed for that. In this thesis, the pulled fiber is termed secondary fiber and the stationary fiber is termed primary fiber (see Figure 2; the horizontal fibers are primary fibers). Usually, shear strength, i.e. the strength needed for breaking the bond parallel to the bonding plane, is measured. Also, out-of-the-plane strength or z-directional strength, torsional or tearing strength and peeling strength have been measured (Saketi 2015). However, this review concentrates on measuring the shear strength.

In the earliest measurement found in the literature, Mayhood et al. (1962) used a modified chainomatic balance with a specially designed bond holder to measure the shear strength. The holder consisted of two metallic plates perpendicular to each other. The other plate was attached to the balance and it had a thin jig with a cut in the middle, and the other plate was stationary and it had a groove for the jig. The bond was fixed on the plates with cement so that the primary fiber was over the groove, the secondary fiber was on the jig, and the bond section stayed above the cut. Schniewind et al. (1964) utilized an Instron tensile tester in a similar measurement. Their holder was a paper strip, whose other end was covered with double-sided adhesive and had a rectangular cut. Stratton and Colson (1990) performed the measurement with a tensile tester specially designed for fibers (FLER2). Their sample holder was made of Mylar plastic sheet and had a U-shaped cut arc in the middle, and the bond was fixed to the holder with Epoxy or hot melt. After fixing the holder to the measurement device, the holder was cut in two in such a manner that the fibers were fixed to different pieces. Magnusson and Östlund (2011) utilized an Instron ElectroPulse E1000 tensile testing machine in their measurement. The metallic sample holder in this work consisted of two parts, and the primary fiber was glued to one part and the secondary fiber to the other. The authors also applied FEM modelling to separate the normal and shear components of the loading. Fischer et al. (2012) used a bond tester comprising two load cells. This way, they could preload the primary fiber before pulling out the secondary fiber. Their bond holder was made of polymer and they fixed the bond to the holder with nail polish. After fixing the holder to the device, they cut it into either two or three

parts with a soldering rod depending on the type of the measurement. The fibers were fixed to separate pieces of the holder after cutting. Saketi and Kallio (2011a) were the first one to apply microrobotics also to this problem. In their approach, the primary fiber was grasped with two microgrippers. The bond was lifted up with the grippers, and the other end of the free secondary fiber was glued on the tip of the force sensor. Saketi and Kallio (2011b) have also demonstrated breaking the bond without the need to use glue. In this method, the other end of the secondary fiber was grasped with a third gripper after grasping the primary fiber with two other microgrippers similarly to Saketi and Kallio (2011a). Figure 2 presents the different methods to fix the bond for the measurements reported in the literature.

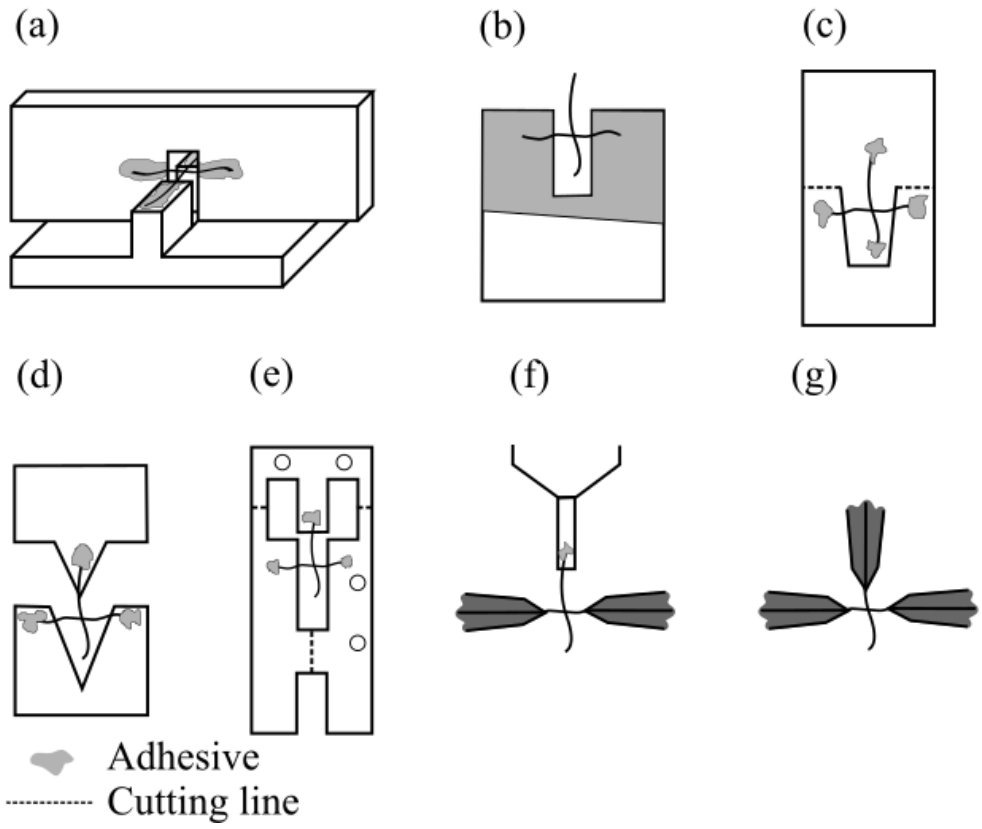

Figure 2. *Bond holder designs by Mayhood et al. (1962) (a), Schniewind et al. (1964) (b), Stratton and Colson (1990) (c), Magnusson and Östlund (2011) (d), Fischer et al. (2012) (e), Saketi & Kallio (2011a) (f), and Saketi & Kallio (2011b) (g). The horizontal fiber is the primary fiber in all of the illustrations.*

2.2.3 **Major Drawbacks**

Often, there is a large variance between the measurement results due to variations in the morphological structure of the fibers (Karlsson 2010). Therefore, a large number of fibers should be measured for meaningful data. In most of the cases, measuring physical properties of individual fibers and bonds requires manual handling of the tiny fiber samples. This is a dexterous and time-consuming step, which requires lots of experience and limits drastically the yield. Manual handling was avoided in some of the works on fiber flexibility by utilizing a channel structure where the fibers flowed in suspension (Meindersma et al. 1961; Olson et al. 1995; Eckhart et al. 2009). However, this approach is applicable solely to the flexibility measurements of the wet fibers. It also isolates the fiber from the surroundings and prevents from measuring other properties such as tensile strength or contact angle from the same fiber. Furthermore, liquid flow is not suitable for manipulating fiber bonds since liquid dissolves the bond.

Automation is needed in the fiber-level measurements to increase repeatability, reliability and yield. The only method that enables automation and still allows multiple measurements on the same fiber or bond is the microrobotic approach introduced by Saketi (Saketi & Kallio 2011a; Saketi & Kallio 2011b; Saketi et al. 2010). The problem with this method is that the platform was tele-operated and thus there still was the need for an experienced operator. The human operator limits the yield as it is hard to interpret the depth and the optimal points to grasp the curly fibers from the camera view. There are two ways to enhance the method: automated microrobotic grasping and computer vision. The first approach answers to the question how to reliably and repeatedly grasp the fibers in an automated manner for the measurements, and the second gives tools for detecting the appropriate fibers, their dimensions and the suitable grasping points from the acquired camera images.

2.3 Novel Approaches

This section describes the novel approaches to automate the fiber-level measurements. Section 2.4.1 presents the recent studies on automated microrobotic grasping to show the different methodologies used for grasping and the variation of samples grasped. The main applications are automated specimen handling and microassembly. Often, different testing parts such as spheres or cubes are used in demonstrating and benchmarking the grasping strategy. Section 2.4.2 discusses the computer vision methods used for extracting information from varying fibers and other thin and elongated objects. The presented studies illustrate the methodologies suitable for paper fiber handling. However, most of them are used only for gathering information from the samples in study, not for manipulation. The major drawbacks and current challenges of automated microrobotic grasping and fiber imaging from the perspective of the needs for automated fiber-level measurements are discussed in Section 2.3.3.

2.3.1 **Automated Microrobotic Grasping**

The strategies for micromanipulation can be divided into two major categories: non-contact and contact. Non-contact methods include electric, magnetic, optic and acoustic means to manipulate objects in air and in liquid (Savia & Koivo 2009). However, the contact methods are more studied and used in the pick-and-place operations in the fields of microrobotics and microassembly. Different approaches from utilizing temperature, vacuum or capillary force to grasping with multiple probes and conventional grippers are found in the literature (Savia & Koivo 2009; Banerjee & Gupta 2013).

In the automated manipulation of microparts, the positions of the part and the grasping tool are usually detected by using an image produced by a conventional light microscope or a scanning electron microscope (SEM), depending on the sizes of the object and the tool. Commonly, there is a priori knowledge of the physical dimensions of the parts, and the locations in the image are detected by utilizing the cross-correlation of the image and templates describing the tool and the object. This process is termed template matching. Also, CAD models can be used in the detection of the part. The coordinate systems of the manipulators i.e. the manipulator frames must be mapped with the image plane coordinates in order to move the manipulator to the desired point in the camera view. The vertical distance between the tool and the part is acquired either from the known dimensions of the part and the known working distance of the tool, or by calculating the distance from the image by using focusing or defocusing algorithms, or by utilizing multiple viewpoints.

The research conducted in automated pick-and-place operations utilizing probes involves works using two probes in the chopstick manner – pioneered by Tanikawa and Arai (1999) –, and works that employ multiple probes for manipulation of parts with challenging geometries. There are also numerous papers that use a single probe for manipulation of microparts by pushing (e.g. (Pawashe & Sitti 2006; Bilen & Unel 2008)) but these works are excluded from this review since the object is not really grasped in those approaches.

Wason et al. (2012) used a platform consisting of two XYZ micromanipulators with tungsten probes and two cameras with microscope optics in automated manipulation tasks of 25 µm thick silicon-on-wafer parts with known 2D dimensions ranging from 100 µm to 700 µm. The first camera was placed on top and its view was utilized in detecting the XY locations of the parts and the probes by applying template matching. The second camera was placed in front with a 20˚ angle, and it was used to detect the depth by utilizing the mirror image produced by the reflective surface. The automated tasks involved grasping and lifting the parts, rotating them about different axes and inserting one of them into a compliant slot.

Xie and Régnier (2009) used two atomic-force microscope (AFM) tips, an XYZ nanopositioning stage and a camera with microscope optics in automated construction of 3D pyramid structures out of microspheres with diameters of 3 and 4 µm. They used the microscope view to detect the spheres

and move the AFM tips to the proximity of the spheres. A special circle detection algorithm was utilized in detecting the spheres. The mapping between the XY planes of the AFM stages and the image axes had been done beforehand. They used the AFM in detecting the grasping points and to give the feedback from the force.

Cappelleri et al. (2012) utilized up to four XYZ micromanipulators with tungsten probes in automated manipulation of seven different 100 µm thick microparts. The microparts were rigid and had 2D dimensions ranging from 75 µm to 580 µm. The platform was constructed on an inverting microscope and it had a tilted side camera for recording the experiments. The probes were detected from the microscope images by applying template matching, and the edges of the microparts were identified by detecting their edges. The optimal grasping points were estimated based on the convex and concave corners of the parts. The image space and the manipulator frames had a common origin and the rotations between the actuator frames and the image space were also known. The experiments involved moving microparts into different 2D formations and lifting and moving them into different 3D formations.

Xing et al. (2014) completed an automated assembly task of four thin irregular-shaped parts with known dimensions ranging from 100 µm to a couple of millimeters. The platform contained three cameras with microscope optics and six XYZ micromanipulators with different probes equipped force sensors. One of the manipulators had also three rotational axes. The parts were detected from the images by using the Hough transform. The objects were moved to the desired positions by moving them until their trackable features reached the desired locations in each view. The force sensors were used in controlling the force in grasping the objects and inserting them together. The mapping between the robot arm frames and the image planes was solved in a calibration step where each robot arm was moved to three different points in each view.

The grippers used in automated grasping can be either active or passive. The opening of the active grippers can be controlled, and they can be also equipped with force sensors to control the grasping force. The shape of the tips of the grippers can be optimized according to the shape of the target object Xie and Régnier (2009). The passive grippers deform and lock to compliant parts when pushed towards the parts. The assembly site has also a similar locking mechanism, and the part locks to the assembly site when pushed to the site. The locking to the assembly site is stronger, and therefore the part is released from the gripper when the gripper is moved away from the site.

Wang et al. (2010) utilized passive microgrippers in automated 3D grasping of microparts with approximate dimensions of 50 µm x 150 µm x 10 µm. The platform consisted of a top camera with microscope optics and an XYZ micromanipulator. The geometries of the parts were known, and they were fixed to a substrate with thin tethers. The passive gripper heads of the micromanipulator were interchangeable and they were utilized to grasp compliant microparts. The microgrippers and the

microparts were detected by template matching. The depth was determined by focusing. The mapping between the image plane and the manipulator frame was determined in a calibration step by moving a part to several locations and tracking the part. The procedure also involved an initialization step, in which the templates for the gripper and the part were selecting from the image, and the gripper was aligned with the first part.

Das et al. (2012) used a reconfigurable platform for two different automated assembly tasks. The first configuration comprised three XYZ micromanipulators with a rotational axis, one XY stage with a rotational axis and a top and a side camera with microscope optics. Two of the micromanipulators had a passive microgripper as an end-effector, and a needle was attached to the third. The second configuration had two XYZ micromanipulators with one rotational axis, one XY stage with a rotational axis, and a top camera. The first configuration was used in assembling 30 microspectrometers each consisting of four parts with thicknesses down to 100 µm. The parts were initially fixed with tethers to specific locations on a substrate, and the parts were picked and moved to the assembly sites, on which they were locked by using snap-connectors. The second configuration was used in assembling 10 eight-legged microrobots from 100 µm thick parts. Also here, the parts were initially in specific locations in the substrate. The legs were grasped with the vacuum grippers and glued into the right locations with the adhesive. The mapping between the manipulator frames and the real-world coordinates was done in a separate step where the user moved the end-effectors to specific locations on a calibration dye. Features were tracked to guide moving the substrates into the picking and the placing locations, and to correct errors in grasping. Otherwise, pick-and-place operations were done without visual feedback.

Zhou et al. (2006) utilized an active XYZ microgripper composed of two fingers capable of independent fine XYZ movements in automated manipulation and inspection of 300µm x 300µm x 100µm microparts. The microrobotic platform consisted of the microgripper, an XY stage and two microscope cameras, one on top and one in front. The inspection task composed of grasping the micropart from the XY stage, lifting it to the focus of the top microscope, and aligning it with the focal plane of the top microscope by rotating the part with the fingers of the microgripper. Grasping was done in feed-forward since the gripper and the part were in predefined positions in the beginning. The part was lifted step-wise until the focus was found based on gradient images. The needed rotations about X and Y axis were detected from the gradient in different quarters of the top view image, and the needed rotation about the Z axis was detected from the edges of the part detected in the top view image.

Tamadazte et al. (2010) used active microgrippers in automated manipulation of 400 µm x 400 µm x 100 µm microparts. The microrobotic platform involved XYZ microgrippers, an XY stage with rotation and a top camera in 45˚ angle. The traceable features and the CAD models of the parts were utilized in finding the poses of the parts from the images. The microparts fitted together and 3D

structures from two and five similar microparts were assembled in the experiments. The position of the camera with respect to the other parts of the platform was known. Also, as an initialization step, the microparts were moved to the desired poses by using tele-operation, and these poses were imaged to set the goal.

Jasper et al. (2011) accomplished automated pick-and-place operations of polymer spheres with approximate diameter of 50 μm on a glass substrate. They used a mobile microrobot equipped with an active microgripper for picking and moving the spheres to desired locations, and a second mobile microrobot equipped with a tungsten probe to assist in releasing the spheres. There were three cameras in the setup: one camera with conventional optics on bottom, one camera with microscope optics on top, and a second camera with microscope optics on side in 45˚ angle. The spheres were detected from the top view by using their circularity. The distance between the tools and the reflective substrate was detected from the side view in the calibration step of the system by utilizing template matching and the mirror image of the tool. The bottom camera was used for tracking the microrobots.

In addition to the fully automated pick-and-place operations and the microassembly scenes, different approaches to facilitate tele-operated micromanipulation have been studied. Fatikow et al. (2007) used the focus level of scanning electron microscope (SEM) to find the depth of a carbon nanotube and a touchdown sensor to sense the contact between the nanogripper and the nanotube. Komati et al. (2013) used a two-finger microgripper with force sensors for secure grasping and moving of a flexible micropart. Bolopion et al. (2012) created a haptic feedback system for grasping spheres to help the user in aligning the gripper head with the sphere. Probst et al. (2009) used multiple view-points together with the CAD models of the parts and the gripping tools to create a virtual reality based graphical user interface with the haptic feedback for collision avoidance for 3D microassembly tasks. Table I summarizes the automated grasping studies presented in this section.

Table I: *Recent automated pick-and-place operations or microassebly tasks found in the literature.*

Study	*Task*	*Tool*	*A priori known of the part*	*Image processing*	*Illumination*
Wason et al. (2012)	Pick-and-place of four microparts	Two probes	2D templates and thickness	Template matching	Coaxial and ring light
Xie & Régnier (2009)	Building 3D structures from microspheres	Two AFM tips	Shape and dimensions	Circle detection	Optical microscope lamp
Cappelleri et al. (2012)	Building 2D and 3D structures of microparts	Four probes	Thickness, rigidity, polygonal shape	Edge detection	Optical microscope lamp
Xing et al. (2014)	Assembling four microparts	Six probes	Part dimensions and features	Hough transform	N/A
Wang et al. (2010)	Grasping and attaching a micropart	Passive gripper	2D templates and thickness	Template matching	Coaxial
Das et al. (2012)	Assembling two different microstructures	Passive gripper / vacuum gripper	Features, picking and placing locations of the parts	Template matching	N/A

Zhou et al. (2006)	Picking up and rotating micro-parts	Active gripper	Shape and dimensions, picking location	Gradient, edge de-tection	Coaxial
Tamadazte et al. (2010)	Assembling a 3D structure with two and five microparts	Active gripper	CAD-models, final posi-tions	Detecting straight lines	Optical mi-croscope lamp
Jasper et al. (2011)	Pick-and-place of microspheres	Active gripper and a probe	Shape and dimensions	Circular maximum filter	Coaxial, reflective surface

The major limitation mentioned in most of the presented studies was the fact that the microrobotic platform and the algorithms were designed for manipulating a specific part and could not be applied to other kinds of objects (Wason et al. 2012; Xie & Régnier 2009; Cappelleri et al. 2012; Xing et al. 2014; Jasper et al. 2011). Creating a microrobotic platform capable of grasping parts with unknown shape and rigidity remains an extremely demanding challenge. Furthermore, the experiments usually consisted of assembling only one part of a component or committing only one task of a process instead of finishing the whole objective (Cappelleri et al. 2012; Wang et al. 2010; Jasper et al. 2011). This shows the effect of the first limitation: often the change of the manipulated object requires major changes in the platform and in the manipulation strategy, and therefore the research has to be started with proof-of-a-concept experiments of one step of the process. The reliability of the grasps is extremely important for getting the systems into more mature stage. To increase the reliability, some papers suggested adding force sensing to the grippers (Cappelleri et al. 2012; Zhou et al. 2006) and working on automated fault diagnostics (Zhou et al. 2006).

2.3.2 **Fiber Imaging**

A common application for fiber imaging is measuring the length and the width of a fiber or another thin and flexible object. As mentioned earlier, there are several commercial devices that measure the length of paper fibers in suspension in high throughput and are capable of online measurements (Hirn & Bauer 2006). These devices measure also other morphological properties such as width,

curliness and wall thickness. In addition, there is a commercial tabletop device for similar measurements of different fibers in laboratory conditions (Fluid Imaging Technologies Inc. 2012). Hou et al. (2005) presented a method to estimate length and width of a paper fiber and to detect the points of maximum curvature from the fiber profile. Adel et al. (2011), Ikiz et al. (2001) and Wang et al. (2008) reported methods to measure the length of multiple cotton fibers in the same image. The methods presented in (Adel et al. 2011; Wang et al. 2008) involved also strategies for detecting some of the cases of overlapping fibers. Other goodness measures such as maturity index and fineness were calculated from the fiber dimensions in (Adel et al. 2011). Shin et al. (2008) studied the diameters of electrospun fibers that formed a web from SEM images. Comin et al. (2014). analyzed the length of muscle fibers and the number of nuclei in them from stained microscope images. (Niemistö et al. 2005) studied the length of veins and the number of junctions between them from the images of cell cultures.

All of these works base on two major steps: distinguishing the fibers and the background and finding the centerline estimate of the fibers. Edge detection was utilized for the measurements of the width or the diameter. The indirect method for measuring the fiber flexibility by Eckhart et al. (2009) mentioned in Section 2.3.1 relied also on the centerline estimate.

Here, the problem was reduced to two-dimensional by the imaging conditions or preparation of the samples. The flow cell based devices have narrow capillaries where the fibers flow in low concentration (Hirn & Bauer 2006; Fluid Imaging Technologies Inc. 2012; Eckhart et al. 2009; Hou et al. 2005). The fibers were trapped between glass slides in (Adel et al. 2011; Ikiz et al. 2001) and put into a special scanner in (Wang et al. 2008). The samples were planar and thin in (Comin et al. 2014; Niemistö et al. 2005) and only a layer of the specimen was analyzed in (Shin et al. 2008). Grasping wet paper fibers can be approximated as a 2D problem as well, since the fibers are staying inside a thin layer of water. However, grasping dry fibers and especially fiber bonds is a clear 3D problem due to the curly nature of paper fibers.

There are also some studies of the 3D imaging of fibers and fiber-like objects. X-ray microtomography (µCT) is widely used in analyzing the 3D topography of paper surface (Chinga-Carrasco et al. 2008) and it has been applied in extracting 3D information of paper and wood fibers as well. Publications include 3D tracking of fibers (Axelsson 2006) and estimation of fiber curvature (Coeurjolly & Svensson 2003) and fiber twist (Aronsson 2002) in 3D images. Byun and Nagata (1996) described a method for determining the 3D pose of a flexible object such as a rope, a wire or a cable from images taken from two different angles with conventional cameras. Kwon et al. (2013) presented a tool for analyzing the movement of a worm in 3D. They used two microscope cameras in specified angles and positions in their setup.

In addition, some work has been done to characterize the fine structure of paper fibers by imaging. Ye et al. (1994) used polarized light in estimation of microfibril orientation, and Kappel et al. (2010a;

2010b) utilized polarized light in measurement of the bonding area. Table II summarizes the studies of the images-based methods to measure different properties of fibers.

Table II: *Summary of the studies on image-based methods of measuring fiber properties.*

Study	*Fiber type*	*Domain*	*Imaging device*	*Measured parameters*
Adel et al. (2011)	Textile	2D	Light microscope with camera	Length, width, area, perimeter (the rest are calculated from these)
Ikiz et al. (2001)	Textile	2D	Light microscope with camera	Length
Wang et al. (2008)	Textile	2D	Fiber scanner	Length, average gray level
Shin et al. (2008)	Industrial	2D	SEM	Diameter (width)
Fluid Imaging Technologies Inc. (2012)	Industrial, paper	2D	High-speed camera in a flow cell	Length, width, area, curl, straightness
Hou et al. (2005)	Paper	2D	High-speed camera in a flow cell	Length, curl
Hirn & Bauer (2006)	Paper	2D	High-speed camera in a flow cell (multiple devices)	Length, width, curl, fibrillation, content, wall thickness, coarseness

Eckhart et al. (2009)	Paper	2D	High-speed camera in a flow cell	Length, flexibility
Comin et al. (2014)	Muscle	2D	Light microscope with camera	Length
Niemistö et al. (2005)	Vein	2D	Light microscope with camera	Length, junctions
Axelsson (2006), Coeurjolly and Svensson (2003), Aronsson (2002)	Paper	3D	µCT	Centerline in 3D, curvature, twist
Byun & Nagata (1996)	Cable	3D	Two cameras	Centerline in 3D
Kwon et al. (2013)	Worm	3D	Two light microscopes with cameras	Centerline in 3D

The centerline estimate is an efficient approach for describing the morphology of thin elongated objects such as fibers. It has been used in estimating the length and the width, finding the curliness, detecting the points of maximum curvature, and tracking of individual fibers in a web or other overlapping structure and finding the junction points. The centerline estimate has been the base in all of the works, only the implementation has varied. The most common method was morphological thinning (Adel et al. 2011; Wang et al. 2008; Shin et al. 2008; Hou et al. 2005; Comin et al. 2014; Niemistö et al. 2005; Byun & Nagata 1996) but also methods based on morphological erosion (Ikiz et al. 2001) and fast marching with corner detection (Eckhart et al. 2009) have been used. Distance transformation (Aronsson 2002; Coeurjolly & Svensson 2003) and radon transform (Axelsson 2006) have been applied in 3D images. Morphological thinning is feasible for all 2D images but high speed requirements might limit its use (Eckhart et al. 2009). Although many different parameters have been measured with computer vision, very little interest in 3D measurements of individual fibers, or manipulating individual fibers or fiber-like objects is seen in the literature.

2.3.3 **Major Drawbacks and Current Challenges**

Most of the studies in automated microrobotic grasping have concentrated on manipulating parts with a known geometry for an assembly process. The part was localized by utilizing templates (Wason et al. 2012; Wang et al. 2010), shape and features (Xie & Régnier 2009; Xing et al. 2014; Zhou et al. 2006; Jasper et al. 2011; Bolopion et al. 2012) or CAD models (Tamadazte et al. 2010; Probst et al. 2009), and its height was known. Therefore, the vision system did not need to be capable of full 3D reconstruction of the part and the scene, and this was not considered in the calibration or mapping of the vision system. Similar prerequisites were involved in grasping. Grasping mechanism or planning was tailored for rigid polygonal parts in (Wason et al. 2012; Cappelleri et al. 2012; Wang et al. 2010; Das et al. 2012; Zhou et al. 2006) or spheres (Xie & Régnier 2009; Jasper et al. 2011). Soft or more complex parts were considered only in (Xing et al. 2014; Komati et al. 2013), and the shape was known beforehand also then. Illumination is crucial in microrobotics and the illumination schemes in all of the studies were tailored for the utilized parts and materials. Illumination relied on the high contrast between the dark parts and the bright substrate in some works (Xie & Régnier 2009; Xing et al. 2014; Zhou et al. 2006; Jasper et al. 2011; Tamadazte et al. 2010), and highlighting the rigid edges in the others (Wason et al. 2012; Cappelleri et al. 2012). These solutions do not work well with the partly transparent thin fibers. In most of the cases, the field of view was quite small (a couple of millimeters x a couple of millimeters) and therefore acquiring even illumination was straightforward. The microrobotic paper fiber experiments have required a 19-mm-high field of view for enough samples to fit in (Saketi et al. 2010; Saketi & Kallio 2011b). This makes designing the illumination even more challenging.

Most of the presented image processing techniques are relevant for analyzing individual paper fibers. However, the imaging setups in all of the studies of microscale fibers were tailored to the particular problem and their usage in a platform for mechanical characterization of paper fibers is problematic. Using a flow cell (Hirn & Bauer 2006; Fluid Imaging Technologies Inc. 2012; Eckhart et al. 2009; Hou et al. 2005), a sandwich structure of two glass slides (Adel et al. 2011; Ikiz et al. 2001), a fiber scanner (Wang et al. 2008), a µCT (Aronsson 2002; Coeurjolly & Svensson 2003; Axelsson 2006) or a limiting camera configuration (Kwon et al. 2013) is not feasible since these setups do not allow simultaneous manipulation of fibers with microrobotic actuators or at least limit significantly their trajectories. In addition, as noted before, most of the imaging systems were applicable only to 2D imaging and could not obtain 3D information required with the dry fibers and bonds. Also here, none of the presented illumination schemes is applicable to microrobotic handling of paper fibers. Furthermore, the goal of the studies discussed was only the analysis of the morphology of inert fibers and fiber-like objects and, in most of the cases, classification based on the morphology. Only in (Byun & Nagata 1996) the motivation laid in manipulating the objects under study although no strategy for achieving this was given. Therefore, no image-based measurements for grasping a fiber or detecting appropriate grasping locations have been presented in the literature.

Automated microrobotic manipulation of paper fibers requires new advances in illumination, computer vision algorithms and microrobotic grasping strategies. The illumination should be appropriate for a microrobotic platform with multiple actuators and enhance the visibility of the fibers in the camera view. Furthermore, the computer vision algorithms should extract morphological information of the fibers and bonds that is relevant for planning of the grasping. Also, the computer vision algorithms should produce 3D data for grasping of dry fibers and bonds, whose 3D geometry is challenging and has high variance. Finally, the grasping strategy should be tailored for flexible fibers with varying morphology instead of rigid parts with known dimensions.

3 Materials and Methods

This chapter discusses the devices and the samples used in the experiments of this thesis work, and describes the mathematical basis of the developed algorithms. Section 3.1 introduces the two microrobotic platforms used for fiber imaging and manipulation. Their components and main applications as well as the stages of the research they are utilized are described. Section 3.2 discusses the fiber samples used in the experiments explaining the types of the fibers and the preparation of the samples. The next sections concentrate on the principles of imaging and extracting metric 3D information from the images. Section 3.3 briefly depicts the homogeneous coordinates commonly used in the mathematics regarding computer vision and multiple view geometry. Section 3.4 introduces the basic projection camera model for mapping the 3D scene to 2D image points. The section discusses in details the adaptations of the model that have been used for the microscope optics and microrobotic systems in the literature. Section 3.5 introduces the methods for camera calibration providing the camera matrices that link the metric 3D points to the image points. Section 3.6 discusses 3D reconstruction, in which images from multiple viewpoints and the camera matrices for those images are used to build a 3D model of the scene imaged. Finally, Section 3.7 presents the morphological thinning method used with the fiber images, and Section 3.8 introduces the pruning method, with which the produces skeleton images were refined.

3.1 Microrobotic Platforms

Two different microrobotic platforms were used in the experiments of the thesis: Fibrobot I and Fibrobot II. The main difference between them is that Fibrobot I has only a top camera (and occasionally a portable side camera to facilitate the work of the operator) whereas Fibrobot II has two tilted top cameras facing against each other and having a 15˚ angle with the horizontal. The two-view camera configuration enables the 3D reconstruction of the imaged scene that is needed with dry fibers and fiber bonds. In addition, the microgripper actuators and the rotary stage have been updated to the versions having a position feedback, and the frame of the platform has been redesigned to allow placing the microscope optics to their working distance. Fibrobot I is more reconfigurable and it has been used in different tele-operated proof-of-concept experiments. Apart from measuring the flexibility of individual fibers (Saketi et al. 2010), making fiber bonds and breaking them (Saketi & Kallio 2011b) and measuring the bond strength (Saketi & Kallio 2011a), it has been used in preparing fiber samples for different microscopy studies (Saketi et al. 2012), measuring the fiber–fiber friction (Saketi et al. 2014), measuring z-directional bond strength (Latifi et al. 2015) and studies on force sensor development (Saketi et al. 2015a; Saketi et al. 2015b; Saketi 2015). Fibrobot II has been designed to be more rigid and suitable for experiments on automation, and the development

of robotic software frameworks for microrobotic handling have been performed on it (Essen et al. 2014). The studies reported in Publications I, II and III of this thesis have been done with Fibrobot I, and Fibrobot II has been utilized in the research presented in Publications IV and V. The reason for this is that Publications I and II are related to 2D measurements and offline data analysis whereas Publications IV and V are connected with 3D measurements and automated protocols. Also, Fibrobot II did not exist while performing the experiments and collecting the data for Papers I, II and III. Publication III discusses 3D calibration and utilizes 3D grasping in validating the calibration results, and a second camera on a tripod was attached to Fibrobot I for that.

Fibrobot I consists of three XYZ micromanipulators, the sample stage and the camera with the microscope optics. Each of the micromanipulators is composed of three piezo-driven linear stages (SLC-1730; SmarAct GmbH, Germany) that use the stick-slip phenomenon. The stages have a 21 mm travel and a 50 nm step width and they are equipped with position sensors with resolution of 1 nm. Different end-effectors can be attached to the micromanipulators. Microgrippers (SG-06-EX; SmarAct GmbH, Germany) are used as the end-effectors for grasping the fibers and bonds. Their maximum opening is 1.0 mm and the jaw thickness is 300 µm. Exchangeable gripper tips with a thickness of 100 µm are attached on the jaws for more accurate grasping. Other end-effectors include a probe for pushing and a microdispenser (PipeJet™ P4.5; BioFluidiX, Germany) for shooting droplets of different test liquids on the fibers. Common configurations are two grippers, three grippers, two grippers and the probe and two grippers and the microdispenser. The fiber samples are placed on the sample stage that is composed of an XY stage and a rotary stage. This way, the fibers can be transported to the range of the micromanipulators and aligned with the grippers for grasping. There are two different sample stage options. Both are built on the same XY stage, which is composed of two perpendicular linear stages (SLC-1760; SmarAct GmbH, Germany) similar to the ones in the XYZ micromanipulators but having a 41 mm range. The first sample stage has a rotary stage (SR-1908; SmarAct GmbH, Germany) with a sample holder made of aluminum. The resolution of the rotary stage is 10 µ˚ and it has a diameter of 19 mm. The sample holder has the same diameter of the stage and there is a well with a diameter of 17 mm and the depth of 100 µm in it. The wet fibers can be kept immersed in a thin layer of water in the well. The second sample stage has a rotary stage with an angle sensor (SR-4513-S; SmarAct GmbH, Germany) and an integrated polarized backlight illumination system. The diameter of the rotary stage is 36 mm, the resolution of rotation is 400 µ˚ and the resolution of the sensor is 15 µ˚. The illumination system is built on the rotary stage and its design and implementation is presented in detail in Publication I. The sample holder is on the illumination system and it is made of glass. There is a 100 µm thick plastic ring-shaped sticker attached on the sample holder to form the well for the wet samples similar to the previous design. The top camera (Manta G-504B; Allied Vision Technologies, Germany) is a monochrome camera and it has a resolution of 2452 x 2056 and a frame rate of 9 fps. It communicates with the computer via gigabit Ethernet. The optics is a tube microscope with motorized zoom and fine focus (12x zoom;

Navitar, USA). The zoom range is 0.58X – 7.00X and the range of the nominal width of the images is 18.97 mm – 1.57 mm, respectively. Fibrobot I is presented in Figure 3.

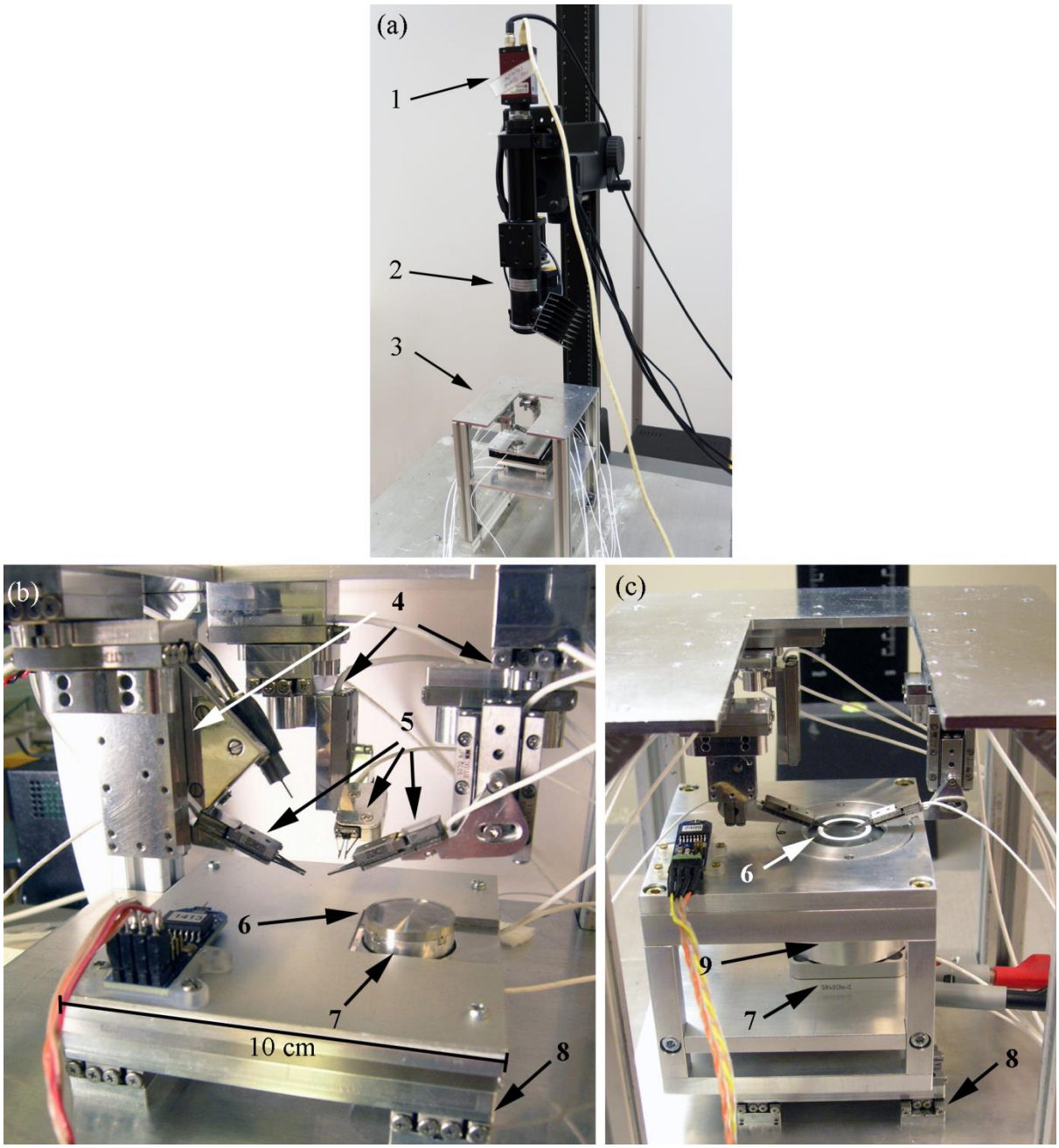

Figure 3. *Fibrobot I. The overall view (a) and two close-ups of different configurations showing the different sample stages (b, c). The camera (1), the microscope optics (2) the frame and the actuators (3), the XYZ micromanipulators (4), the microgrippers (5), the sample holder (6), the rotary stage (7), the XY stage (8), and the illumination system (9).*

Fibrobot II is composed of three XYZ micromanipulators, a sample stage and two tilted top cameras with the microscope optics. The cameras are facing against each other and they have a 15˚ angle with the horizontal and hence the difference between the image planes is 30˚. The camera angle was chosen to be as small as possible still allowing approximately the same field of view for the both cameras. The dimensions of the optics limited the angle. The small angle between the views facilitates the detection of the correspondences between them. The micromanipulators are similar to the ones in Fibrobot I. The only end-effectors used in the experiments have been the microgrippers (SG-1730-M; SmarAct, Germany). These microgrippers have been built on the similar linear stages as used in the XYZ micromanipulators and they thus have position sensors. Therefore, they are more compatible to the automated opening and closing. The gripper jaws are interchangeable and their thickness is 250 µm. Dot grid patterns have been glued on the gripper jaws to facilitate tracking the grippers in the images. The patterns were fabricated by exposing photographic paper under a precise microlithography mask (Micro Lithography Services Ltd., UK) and using standard developing chemicals (developer, stop bath and fixer) in a normal darkroom. The diameter and the spacing of the dots is 75 µm and 250 µm, respectively. The sample stage is the one with the integrated illumination described above and depicted in Figure 3c. The cameras are similar to the one used in Fibrobot I and the optics are newer versions of the one in Fibrobot I. The both optics have also integrated polarizers. Figure 4 shows Fibrobot II.

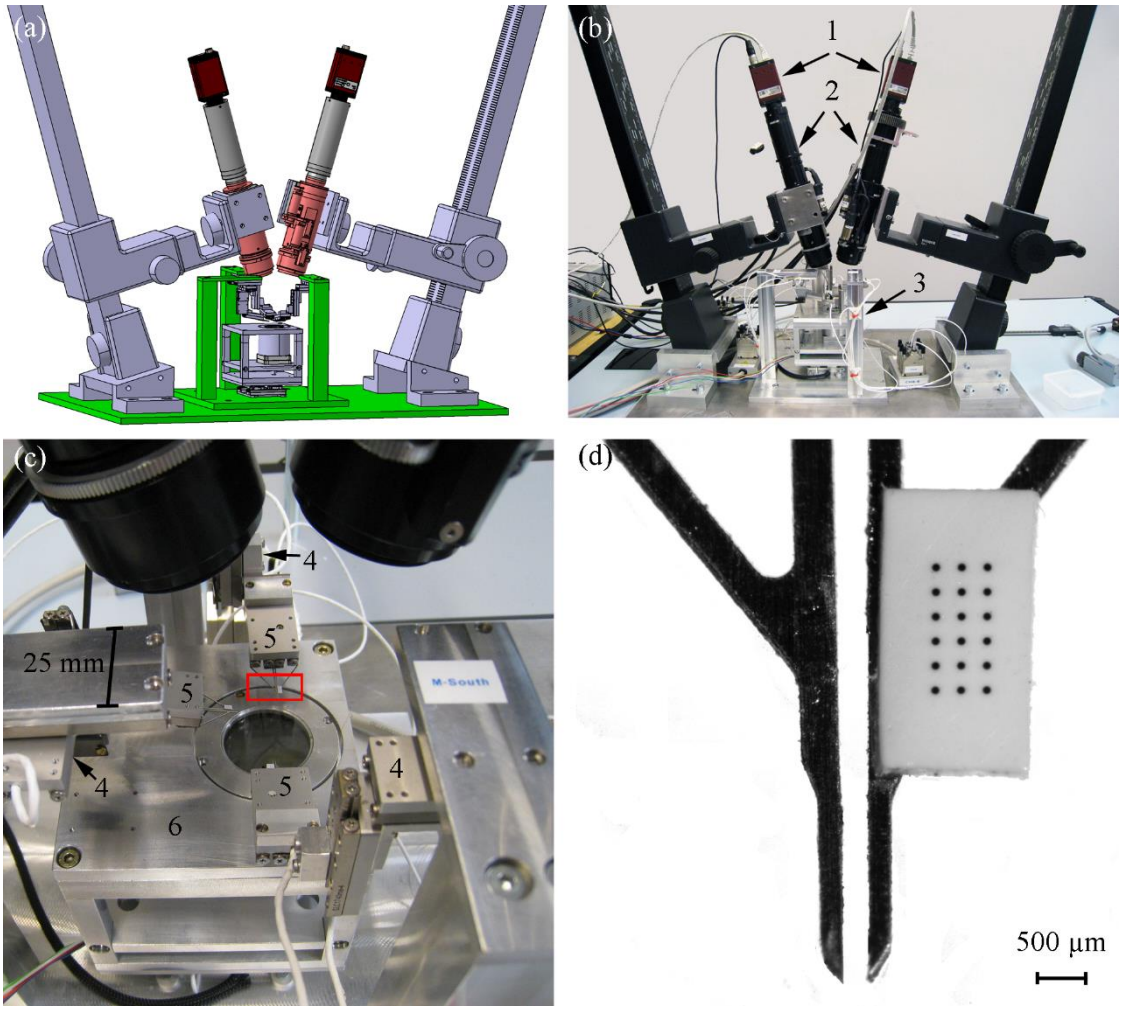

Figure 4. *Fibrobot II. The CAD drawing (a), the overall view (b), the close-up of the actuators (c), and the close-up of the gripper jaws with the dot pattern (d). The area of the close-up in (d) is surrounded by a red rectangle in (c). The cameras (1), the microscope optics (2), the frame and the actuators (3), the XYZ micromanipulators (4), the microgrippers (5), and the sample stage (6).*

3.2 Fiber Samples

The paper fiber samples that have been used in this thesis have primarily been non-recycled unbleached softwood kraft pulp. The fibers have been stored as pulp sheets in a fridge, and the fibers have been disintegrated from the sheet by diluting a piece of the sheet in deionized water. The resulting suspension has been dispensed into the well of the sample holder with a pipette to acquire wet paper fibers needed in Publication I and Publication II. The excess water has been removed with a pipette to maintain the surface flat. The suspension is shown in Figure 5 and a microscope image of individual wet fibers is presented in Figure 7a.

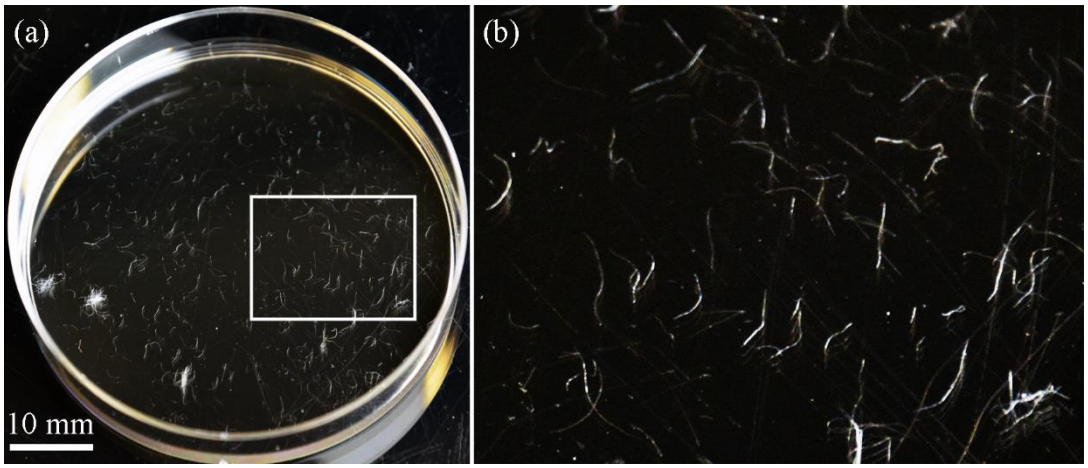

Figure 5. *Fiber samples in deionized water in a Petri-dish. Overall view (a) and a close-up of the area surrounded by the white rectangle (b)*

The dry paper fibers needed in Publication III and IV have been obtained by dispensing the suspension on Teflon plates and letting the water evaporate. Then, the individual dry fibers have been collected manually with pincers. Figure 6 presents dried fiber samples on a Teflon plate and Figure 7b shows an individual dry fiber. Sometimes, the fibers become remarkably twisted while drying as it can be seen from Figure 7b.

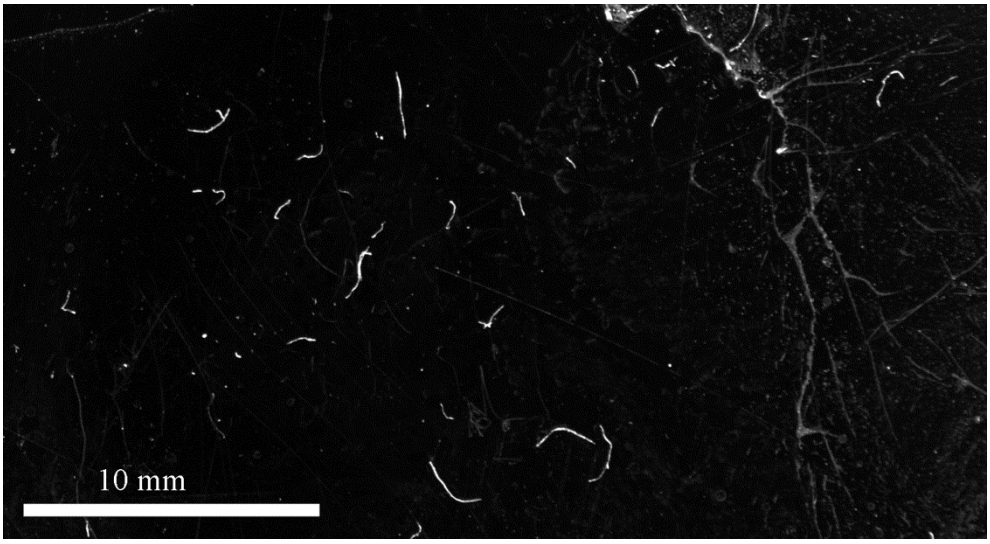

Figure 6. *Fiber samples dried on a Teflon plate.*

The fibers had to stay still between two measurements in Publication IV. The dry fibers were molded in Sylgard 184 polydimethylsiloxane (PDMS) (Dow Corning, USA) in order to achieve this. PDMS is a thermally curable two-component elastomer with medium viscosity. PDMS is transparent for wavelengths from 240 nm to 1100 nm (McDonald & Whitesides 2002) and therefore it does not limit the view to the sample and is appropriate for imaging with the polarized backlight. The ratio between the base and the curing agent was 10:1. We poured approximately a 1mm-thick layer of PDMS into a Petri-dish, placed the fibers in it with pincers, put the mixture inside a vacuum to remove the gas bubbles from the PDMS, and placed the mixture in a 60˚C oven for four hours. We cut out roughly 4–6 mm^2 regions containing individual fibers from the solid PDMS with a scalpel.

The bonds needed for Publication V were obtained by diluting the suspension on a Teflon plate, placing another Teflon plate and a 42 N load on the first one, and maintaining the structure in a 70˚C oven for an hour. This caused the overlapping fibers to bond together. The bonds were detected manually and collected with pincers. Figure 7c shows a microscope image of an individual dry fiber bond.

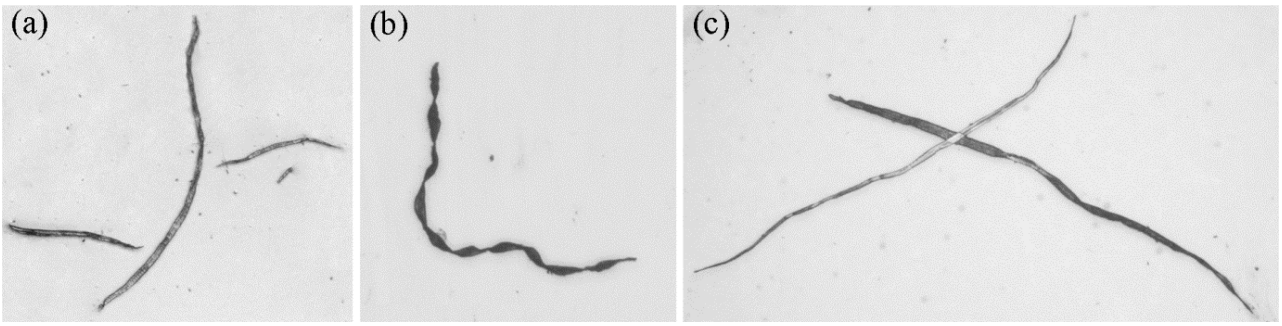

Figure 7. *Individual wet fibers (a), an individual dry fiber (b) and a dry fiber bond (c).*

3.3 Homogeneous Coordinates

Homogeneous coordinates are commonly used in the fields of projective geometry and computer graphics. They allow representing common coordinate transformations such as projection, rotation and scaling as matrix – vector multiplications. The only difference between the Cartesian coordinates and the homogeneous coordinates is that the homogeneous coordinates include also the scale as the last element. In this thesis, Cartesian 2D and 3D coordinates are presented as

$$\mathbf{m} = \begin{bmatrix} x & y \end{bmatrix}^T, \quad \mathbf{M} = \begin{bmatrix} X & Y & Z \end{bmatrix}^T \tag{1}$$

and the homogeneous coordinates are presented as

$$\tilde{\mathbf{m}} = \begin{bmatrix} x & y & w \end{bmatrix}^T, \quad \tilde{\mathbf{M}} = \begin{bmatrix} X & Y & Z & W \end{bmatrix}^T, \tag{2}$$

where *w* and *W* stand as the scale and they are commonly set as 1. In the case of image points, *u* and *v* are used instead of *x* and *y*.

3.4 Camera Mapping

Camera maps the 3D scene to the 2D image. This mapping can be estimated with a camera model. The simplest and the most-used model is the basic pinhole camera model. It describes how the 3D point $\mathbf{M} = [X, Y, Z]^T$ in the Euclidean coordinate system is projected on a plane at $Z = f$ when the center of projection is the origin of the coordinate system. The center of projection is also called the camera center, and the plane is called the image plane. Under these conditions, **M** is mapped to the intersection of the line joining **M** with the center of projection and the image plane. The model is shown in Figure 8. The point $\mathbf{M} = [X, Y, Z]^T$ is mapped to the point $\mathbf{m} = [\mathrm{f}X/Z, \mathrm{f}Y/Z]^T$ on the image plane by the similar triangles as seen in Figure 8b. (Hartley & Zisserman 2004, pp. 153-166).

With the homogeneous coordinates, the pinhole camera mapping is presented as follows

$$\tilde{\mathbf{m}} = \mathbf{P}\tilde{\mathbf{M}} \tag{3}$$

$$\begin{bmatrix} fX/Z \\ fY/Z \\ 1 \end{bmatrix} = \begin{bmatrix} f & 0 & 0 & 0 \\ 0 & f & 0 & 0 \\ 0 & 0 & 1 & 0 \end{bmatrix} \begin{bmatrix} X \\ Y \\ Z \\ 1 \end{bmatrix} \tag{4}$$

and **P** is called the camera matrix. The camera matrix can be decomposed to a product of two matrices describing the intrinsic and extrinsic properties of the camera:

$$\mathbf{P} = \mathbf{K}\left[\mathbf{R} \mid \mathbf{t}\right]. \tag{5}$$

K is the calibration matrix and it describes the intrinsic properties of the camera. The pose of the camera is defined by the rotation matrix **R** and the translation vector **t**. The rotation matrix is defined as follows

$$\begin{aligned}\mathbf{R} = \mathbf{R}_z(\alpha)\mathbf{R}_y(\beta)\mathbf{R}_x(\gamma) &= \begin{bmatrix}\cos\alpha & -\sin\alpha & 0\\ \sin\alpha & \cos\alpha & 0\\ 0 & 0 & 1\end{bmatrix}\begin{bmatrix}\cos\beta & 0 & \sin\beta\\ 0 & 1 & 0\\ -\sin\beta & 0 & \cos\beta\end{bmatrix}\begin{bmatrix}1 & 0 & 0\\ 0 & \cos\gamma & -\sin\gamma\\ 0 & \sin\gamma & \cos\gamma\end{bmatrix}\\ &= \begin{bmatrix}\cos\alpha\cos\beta & \cos\alpha\sin\beta\sin\gamma - \sin\alpha\cos\gamma & \cos\alpha\sin\beta\cos\gamma + \sin\alpha\sin\gamma\\ \sin\alpha\cos\beta & \sin\alpha\sin\beta\sin\gamma + \cos\alpha\cos\gamma & \sin\alpha\sin\beta\cos\gamma - \cos\alpha\sin\gamma\\ -\sin\beta & \cos\beta\sin\gamma & \cos\beta\cos\gamma\end{bmatrix},\\ &= \begin{bmatrix}r_{11} & r_{12} & r_{13}\\ r_{21} & r_{22} & r_{23}\\ r_{31} & r_{32} & r_{33}\end{bmatrix}\end{aligned} \tag{6}$$

where *α*, *β* and *γ* are the rotation angles about Z, Y and X axis, respectively. The translation vector is defined

$$\mathbf{t} = \begin{bmatrix}t_x & t_y & t_z\end{bmatrix}^T, \tag{7}$$

where t_x, t_y and t_z are the translations in X, Y and Z axis, respectively. In the case depicted in Figure 8, the image plane is parallel to the XY plane of the imaged scene and the origin of the imaged scene is set to the camera center. Thus, there is no rotation or translation between the camera coordinate system and the world coordinate system, and **R** = diag(1, 1, 1) and **t** = **0**. As the camera is a perfect pinhole camera and therefore has **K** = diag(*f*, *f*, 1), the camera matrix **P** gets the form shown in (4). However, there are three possible imperfections in the CCD cameras. First, the principal point is not necessarily in the center of the image plane, i.e. the CCD image sensor, due to the inaccuracies in attaching the sensor to the camera. Second, the sensor is composed of pixels and they are not necessarily square. Third, the *u* and *v* axis may not be perpendicular to each other. Considering these points, the calibration matrix gets the form

$$\mathbf{K} = \begin{bmatrix} fm_x & s & m_x p_x \\ 0 & fm_y & m_y p_y \\ 0 & 0 & 1 \end{bmatrix} = \begin{bmatrix} \partial_x & s & u_0 \\ 0 & \partial_y & v_0 \\ 0 & 0 & 1 \end{bmatrix} \tag{8}$$

where p_x and p_y are the x and y coordinate of the principal point, m_x and m_y are the transformation factors from the world coordinates to the pixel coordinates in the x and y directions and s is the skew factor relating to the angle between the u and v axis (Hartley & Zisserman 2004, pp. 153-166). However, it is common to assume that $m_x = m_y = m$ and $s = 0$ due to the high standards of modern cameras. Then, the explicit form of (5) is as follows

$$\begin{bmatrix} u \\ v \\ 1 \end{bmatrix} = \begin{bmatrix} fm & 0 & mp_x \\ 0 & fm & mp_y \\ 0 & 0 & 1 \end{bmatrix} \begin{bmatrix} r_{11} & r_{12} & r_{13} & t_x \\ r_{21} & r_{22} & r_{23} & t_y \\ r_{31} & r_{23} & r_{33} & t_z \end{bmatrix} \begin{bmatrix} X \\ Y \\ Z \\ 1 \end{bmatrix} \tag{9}$$

More complex versions of **K** exist in the literature. The interested reader is guided to read e.g. (Kannala et al. 2009).

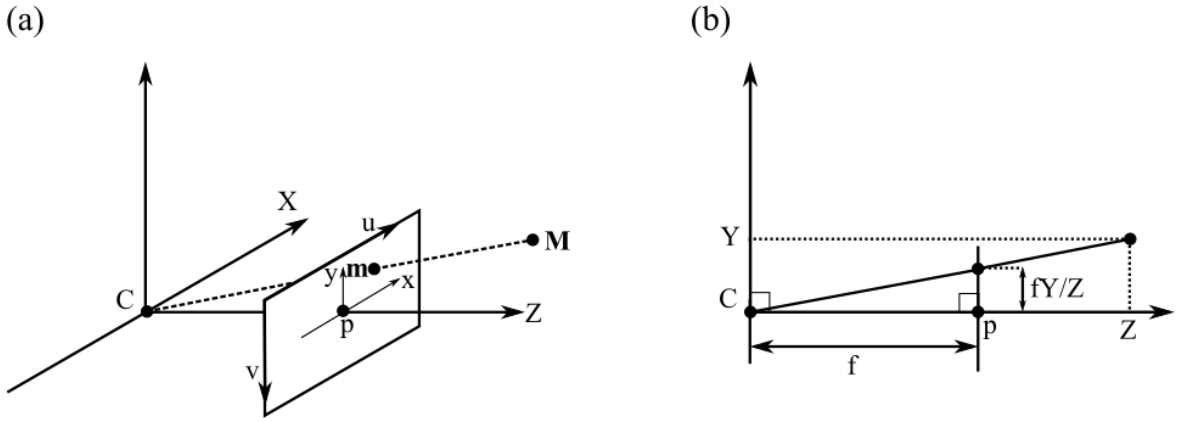

Figure 8. *Pinhole camera geometry. 3D view (a) and YZ plane (b). C is the camera center and p is the principal point. Adapted from (Hartley & Zisserman 2004, p. 54).*

Apart from the possible imperfections of the image sensor, the basic pinhole camera model does not consider the possible distortion caused by the lens. The most common distortions are radially symmetric due to the symmetry of the lens and thus removing radial distortion is an essential step in camera calibration. The radial distortion increases with the distance from the center of the lens and it is defined as follows:

$$u'' = (u - u_0)(1 + k_1 r^2 + k_2 r^4) \tag{10}$$

$$v'' = (v - v_0)(1 + k_1 r^2 + k_2 r^4), \tag{11}$$

where *r* is the radial distance from the center of radial distortion (Heikkilä & Silven 1997). If the center is assumed to be at the principal point, $r^2 = (u - u_0)^2 + (v - v_0)^2$.

3.4.1 **Adaptations to Microscope Optics and Microrobotic Systems**

The common simplification for microscope camera systems is to regard the mapping as a bare plane transformation due to the very narrow depth of field of the microscopes. Now, all the world coordinates are on a single plane termed the object plane. It is further assumed that the image plane is nearly parallel to the object plane. This is usually the case with the microscope camera systems and it suits well the microrobotic applications where the parts to be manipulated have known dimensions and they can be treated as the lie on the object plane. Hence, the Z coordinate will be constant for all the X and Y coordinates and it can be set to zero for computational convenience. Then, (9) will be reduced to.

$$\begin{bmatrix} u \\ v \\ 1 \end{bmatrix} = \begin{bmatrix} fm_x & 0 & m_x p_x \\ 0 & fm_y & m_y p_y \\ 0 & 0 & 1 \end{bmatrix} \begin{bmatrix} r_{11} & r_{12} & t_x \\ r_{21} & r_{22} & t_y \\ r_{31} & r_{32} & t_z \end{bmatrix} \begin{bmatrix} X \\ Y \\ 1 \end{bmatrix}. \tag{12}$$

Sitti and Hashimoto (1999) used a planar transformation model to solve the small misalignment between the manipulator XY plane and the image plane. Other rotations were assumed to be insignificant. Therefore, they considered only the rotation about Z axis with separate values for the angles between X and u axes and Y and v axes, marked here as α_x and α_y. Their model did not solve the actual camera matrix and the transformation was defined from the pixel coordinates to the actuator coordinates with the pixel-to-metric transformation coefficients η_x and η_y. They did not consider the radial distortion. Wang et al. (2010) used similar model in their work. Here, the mapping from the image plane to the object plane is defined

$$\begin{bmatrix} X \\ Y \end{bmatrix} = \begin{bmatrix} \eta_x \cos\alpha_x & -\eta_y \sin\alpha_y \\ \eta_x \sin\alpha_x & \eta_y \cos\alpha_y \end{bmatrix} \begin{bmatrix} u \\ v \end{bmatrix}. \tag{13}$$

Zhou and Nelson (1999) modified (12) by dividing the focal length to the focal length of the lens f_{ob} and the microscope tube length f_{TL} with a substitution $f = (f_{ob} + f_{TL})$. They also claimed that due to the limited depth of view, the distance from the object to the lens is the sum of the focal length and the small gap between the focal plane and the object plane d. Thus, $t_z = f + d$. Taken these together, the result is as follows

$$\begin{bmatrix} u \\ v \\ 1 \end{bmatrix} = \begin{bmatrix} (f_{TL} + f_{ob})m_x & 0 & m_x p_x \\ 0 & (f_{TL} + f_{ob})m_y & m_y p_y \\ 0 & 0 & 1 \end{bmatrix} \begin{bmatrix} r_{11} & r_{12} & t_x \\ r_{21} & r_{22} & t_y \\ r_{31} & r_{32} & f + d \end{bmatrix} \begin{bmatrix} X \\ Y \\ 1 \end{bmatrix}. \tag{14}$$

Actually, their model defined u and v in the metric units from the principal points, and therefore $m_x = m_y = 1$ and $p_x = p_y = 0$. They considered also the radial distortion in later steps.

Ammi et al. (2009) simplified the rotation matrix of the model in (14). Since the object plane is estimated to be nearly parallel to the image plane, the rotation angles $\beta = \gamma \approx 0$. Hence, they approximated $\cos\beta = \cos\gamma \approx 1$ and $\sin\beta \approx \beta$ and $\sin\gamma \approx \gamma$. This yields the following mapping

$$\begin{bmatrix} u \\ v \\ 1 \end{bmatrix} = \begin{bmatrix} (f_{TL} + f_{ob})m_x & 0 & m_x p_x \\ 0 & (f_{TL} + f_{ob})m_y & m_y p_y \\ 0 & 0 & 1 \end{bmatrix} \begin{bmatrix} \cos\alpha & -\sin\alpha & t_x \\ \sin\alpha & \cos\alpha & t_y \\ -\beta & \gamma & t_z \end{bmatrix} \begin{bmatrix} X \\ Y \\ 1 \end{bmatrix}. \tag{15}$$

Since they used the similar pinhole microscope model as Zhou and Nelson, the substitution $t_z = f + d$ holds for (15) as well. However, they were not interested in solving the parameter d and thus did not use it in the model. They also considered the radial distortion in their study.

Bilen et al. (2012) did not divide the focal length into its factors. They interpreted the assumption for the image plane and the object plane being nearly parallel by applying the approximations $r_{31} = r_{32} = 0$. They used the average distance between the sample and the objective $\bar{d}$ as t_z, which is a similar approximation to $t_z = f + d$ used in (14). Their work did not consider the radial distortion. The transformation from the object plane to the image plane is now defined as

$$\begin{bmatrix} u \\ v \\ 1 \end{bmatrix} = \begin{bmatrix} fm_x & 0 & m_x p_x \\ 0 & fm_y & m_y p_y \\ 0 & 0 & 1 \end{bmatrix} \begin{bmatrix} r_{11} & r_{12} & t_x \\ r_{21} & r_{22} & t_y \\ 0 & 0 & \overline{d} \end{bmatrix} \begin{bmatrix} X \\ Y \\ 1 \end{bmatrix}. \tag{16}$$

Tamadazte et al. (2008) modified (12) for microscopes with multiple magnifications. They assumed the pixels to be square. Their model treated the pixel transformation factor *m* as a function of the zoom factor ζ. They claimed the radial distortion to be so weak in the modern microscopes that it can be neglected. Their model was as follows

$$\begin{bmatrix} u \\ v \\ 1 \end{bmatrix} = \begin{bmatrix} fm(\zeta) & 0 & m(\zeta)p_x \\ 0 & fm(\zeta) & m(\zeta)p_y \\ 0 & 0 & 1 \end{bmatrix} \begin{bmatrix} r_{11} & r_{12} & t_x \\ r_{21} & r_{22} & t_y \\ r_{31} & r_{32} & t_z \end{bmatrix} \begin{bmatrix} X \\ Y \\ 1 \end{bmatrix}. \tag{17}$$

As seen, a few adaptations of the basic pinhole camera model for purposes of microscopy and microrobotics exist in the literature. The differences in the presented models lay in the level of simplification of the rotation matrix and in the details of describing the focal length. However, the main point in all of the adaptations is to reduce the pinhole model for imaging planar scenes only. Extracting varying depth information from the same image with the model is not considered.

3.5 Camera Calibration

Camera calibration or camera resectioning is done to solve the parameters of the camera model. If only the mapping from the 3D scene to the image plane is required, it is enough to solve the parameters of the 3 x 4 camera matrix **P** without the decomposition into the intrinsic and the extrinsic parameters. After the camera calibration, it is possible to perform metric measurements from the image and to compute the position of the camera related to the imaged scene. If there are at least two cameras and their camera matrices are known, the 3D points of the features imaged with both cameras can be calculated. The main purpose of the camera calibration in microrobotic systems is to map the image points with the manipulator frame(s). This enables automated manipulation of the targets in the camera view. For clarification, Figure 9 shows the image planes and the manipulator frames of Fibrobot II presented in Section 3.1. There are two image planes $\{C_1\}$ and $\{C_2\}$ for the cameras, and three manipulator frames $\{M_N\}$, $\{M_W\}$ and $\{M_S\}$ for the XYZ micromanipulators (subscripts standing for north, west and south).

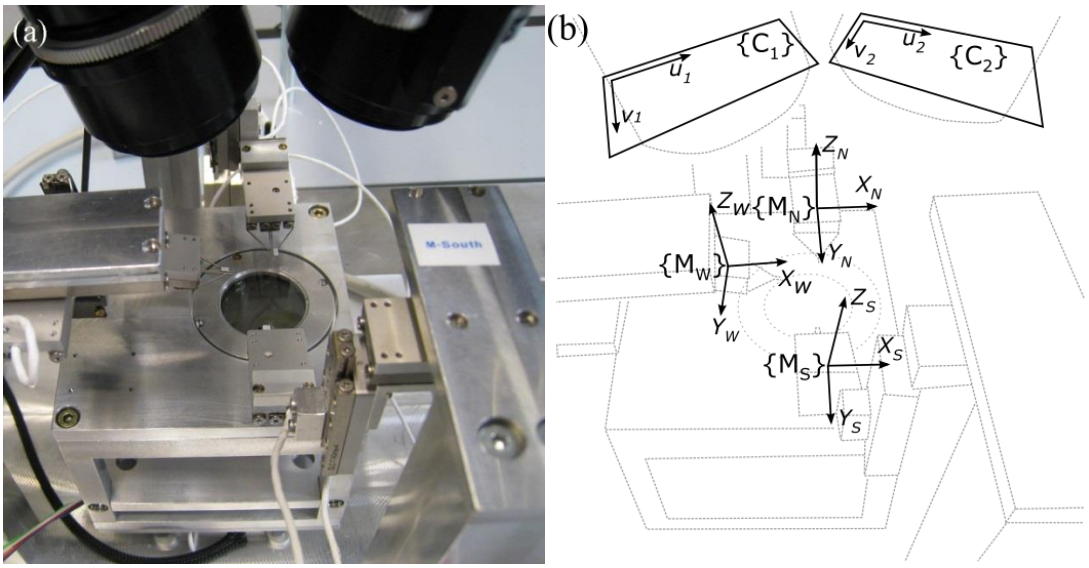

Figure 9. *The image planes and the manipulator frames of Fibrobot II are seen in (b). Picture of Fibrobot II is presented in (a) for clarification.*

The existing calibration techniques can be divided roughly into three categories: photogrammetric calibration, multiplane calibration and self-calibration (Zhang 2000). Photogrammetric calibration uses correspondences between the known 3D points and the image points to solve the required parameters. Self-calibration utilizes correspondences between the images taken from a rigid scene with a moving camera. Multiplane calibration is an intermediate between these two and it uses several images of a planar pattern in different orientations created either by moving the pattern or the camera. Multiplane calibration is the most commonly used method with standard cameras and open source calibration toolboxes exist for software such as Matlab and OpenCV (Bouguet; Bradski & Kaehler 2008).

Photogrammetric calibration is the most useful for the applications with a microscope. The camera motion needed in self-calibration is not practical with the microscopes. Moving a planar pattern to different orientations under the field-of-view of a microscope is also a cumbersome and pain-staking task. Moreover, the errors in multiplanar calibration are high with orientations lower than 30˚ between the calibration pattern and the image plane (Zhang 2000). Such high angles are hard to achieve due to the narrow depth of field of microscopes.

The 3D points needed in photogrammetric calibration can be acquired using a calibration object with known equidistant high-contrast features such as chessboard pattern or dots, or moving an actuator in the camera view, tracking an interest point on the actuator and using the position sensor data. The 3D calibration objects used in the microscale include a black triangular prism with white dots

printed to its sides (Edwards et al. 2000), a staired 3-µm-high pyramid with nanomarkers milled on its stairs (Ritter et al. 2004) and water droplet covered with nickel fillings (Bert et al. 2007). Since the microscope camera is often modelled as a planar mapping, 2D calibration objects are used as well. They are easier to manufacture than the 3D objects but do not give any depth data. Patterns consisting of black squares on a white background (Zhou & Nelson 1999), black dots on a white background (Estaña et al. 2004) and straight lines sputtered of gold (Wason et al. 2012) have been used. The advantage of a calibration object is that only one image is needed to calibrate the camera. However, manufacturing the calibration object is a challenging and expensive task and requires special equipment. Moreover, fitting the calibration object into the field of view is problematic in setups with limited space. Furthermore, the mapping between the actuator frames and the coordinate system of the calibration object has to be done in a separate step.

Utilizing the actuator(s) of the setup in camera calibration removes the need for an external calibration object and provides the mapping between the image plane and the actuator frame at once. Mostly 2D trajectories have been used in microrobotic setups (Sitti & Hashimoto 1999; Bilen & Unel 2008; Tamadazte et al. 2008; Wang et al. 2010) but also some 3D trajectories are found from the literature (Kawaji et al. 2001; Ammi et al. 2009). Also, the 3D trajectory in (Ammi et al. 2009) actually consists of two planes that are parallel to the image planes of the two cameras of the setup and only coplanar points are used in calibration of the cameras.

When the correspondences between the real world and the image points have been acquired, there are different methods to calculate the needed parameters. If the radial distortion is not considered, the problem is simplified to solving a set of linear equations. There are basically two techniques used for this. These techniques are valid for the 3 x 4 transformation matrix described in (9) as well as for the 3 x 3 transformation matrices depicted in (12) – (17). The first one is linear least squares (LLS). The set of transformation equations is reorganized to the form

$$\mathbf{Q}\mathbf{p} = \mathbf{b}\,. \tag{18}$$

The elements of the matrix **Q** consist of the combinations of the 3D points and the image points and constants, the vector **b** consists of the image points and the terms of the camera matrix are in vector **p**. The least squares solution of vector **p** is then solved by fixing one of its elements and continuing as follows:

$$\mathbf{p} = \left(\mathbf{Q}^T\mathbf{Q}\right)^{-1}\mathbf{Q}^T\mathbf{b}\,. \tag{19}$$

The extrinsic and intrinsic parameters are then extracted by applying certain constraints if needed (Salvi et al. 2002). This technique has been used for microrobotic systems in (Sitti & Hashimoto 1999; Wang et al. 2010). If the radial distortion is considered, the computation is done in two steps. The first step is linear and it yields an estimate of the extrinsic parameters. The second step is the non-linear optimization and it produces the intrinsic parameters. Finally, the extrinsic parameters are refined. One of the most widely used techniques for this is the Tsai's method (Tsai 1987; Salvi et al. 2002). Modifications of it have been used for microscope systems in (Zhou & Nelson 1999; Bilen & Unel 2008)

Another linear technique is the direct linear transformation (DLT) (Sutherland 1974). Here, the equations between the correspondence points are organized as

$$\mathbf{Ap} = \mathbf{0}. \tag{20}$$

Now, all the measurement data is in the matrix **A**, and **p** consists of the terms of the camera matrix. To avoid the trivial solution **p** = **0**, additional constraint, e.g. ||**p**|| = 1, is needed. Applying singular value decomposition (SVD) to **A** yields

$$\mathbf{A} = \mathbf{USV}^T \tag{21}$$

and **p** is the last column of **V**. The extrinsic and intrinsic parameters can be calculated from the elements of **p** using matrix algebra and certain constraints (Zhang 2004). If the radial distortion is considered, the second non-linear step and the refining step are required here as well (Zhang 2004). This kind of approach was used for a microrobotic system in (Ammi et al. 2009).

The advantage of DLT is that the computation of the error-sensitive term $\mathbf{Q}^T\mathbf{Q}$ is avoided (Inkilä 2005). Least squares method is a faster technique but that is not usually a big advantage when working with the modern computers. Next, the DLT method is discussed in more details.

3.5.1 Direct Linear Transformation Algorithm

Direct linear transformation (DLT) is a convenient method to solve the transformation matrix between two sets of homogeneous coordinates. In the publications of this thesis, it has been used to calculate the camera matrix from image point – 3D point correspondences. We start from the basic equation of camera matrix shown in (3). It can be expressed as a cross-product and written explicitly as

$$\tilde{\mathbf{m}} \times \mathbf{P}\tilde{\mathbf{M}} = \begin{bmatrix} v\mathbf{p}^{3}\tilde{\mathbf{M}} - w\mathbf{p}^{2}\tilde{\mathbf{M}} \\ w\mathbf{p}^{1}\tilde{\mathbf{M}} - u\mathbf{p}^{3}\tilde{\mathbf{M}} \\ u\mathbf{p}^{2}\tilde{\mathbf{M}} - v\mathbf{p}^{1}\tilde{\mathbf{M}} \end{bmatrix} = \mathbf{0}, \tag{22}$$

where $\mathbf{p}^i$ is the ith row of **P**. Since the three equations are linearly dependent, only two are needed. The first two yield

$$\begin{bmatrix} \mathbf{0}^T & -w\tilde{\mathbf{M}}^T & v\tilde{\mathbf{M}}^T \\ w\tilde{\mathbf{M}}^T & \mathbf{0}^T & -u\tilde{\mathbf{M}}^T \end{bmatrix} \begin{bmatrix} \mathbf{p}^{1T} \\ \mathbf{p}^{2T} \\ \mathbf{p}^{3T} \end{bmatrix} = \mathbf{0}. \tag{23}$$

This is now the form given in (20) with

$$\mathbf{A} = \begin{bmatrix} \mathbf{0}^T & -w\tilde{\mathbf{M}}^T & v\tilde{\mathbf{M}}^T \\ w\tilde{\mathbf{M}}^T & \mathbf{0}^T & -u\tilde{\mathbf{M}}^T \end{bmatrix}. \tag{24}$$

Therefore, each image point – 3D point correspondence yields two equations for solving **P** and thus adds two rows to the matrix **A**. Since there are 11 linearly independent elements in **P**, at least 5½ points are needed (only u or v is required from the sixth). However, using more points increases reliability as the image point data will not be exact. Then again, when more points are used, there will not be an exact solution for (23) since the system is over-determined. Applying singular value decomposition (SVD) to **A** with a constraint ||**p**||=1 yields (21) and **p** is the last column of **V**. (Hartley & Zisserman 2004, pp. 178-181).

As mentioned, the data in the matrix **A** is not ideal due to the noise and measurement errors. Therefore, the solution will always be an approximation, which minimizes the square sum of the error between **A** and $\mathbf{USV}^T$. It is thus essential that the elements of **A** must have similar magnitude. This is why the image points and the 3D points should be normalized before applying DLT. Here, the centroid of the points is translated to the origin and their coordinates are scaled so that their average distance from the origin is $\sqrt{2}$ in the case of the image points and $\sqrt{3}$ in the case of the 3D points (Hartley & Zisserman 2004, pp. 178-181). This is achieved with appropriate similarity transformations **T** and **L** as follows

$$\mathbf{m}_i^N = \mathbf{T}\mathbf{m}_i \tag{25}$$

$$\mathbf{M}_i^N = \mathbf{L}\mathbf{M}_i . \tag{26}$$

After calculating the camera matrix $\mathbf{P}^N$ with the normalized points $\mathbf{m}_i^N$ and $\mathbf{M}_i^N$ by using DLT, the result has to be denormalized to yield the camera matrix **P** for the original points $\mathbf{m}_i$ and $\mathbf{M}_i$

$$\mathbf{P} = \mathbf{T}^{-1}\mathbf{P}^N\mathbf{L} . \tag{27}$$

3.6 3D Reconstruction

3D reconstruction is a technique to calculate the 3D points from the corresponding image points between two calibrated cameras. Basically, this is based on triangulation. As Figure 8 shows, the pinhole camera model describes the image point as the intersection of the image plane and the ray going from the 3D point to the camera center. Thus, the image point can be back-projected to the ray by using the camera matrix. When there are two cameras, the 3D point can be detected as the intersection of the two rays. Figure 10 clarifies this.

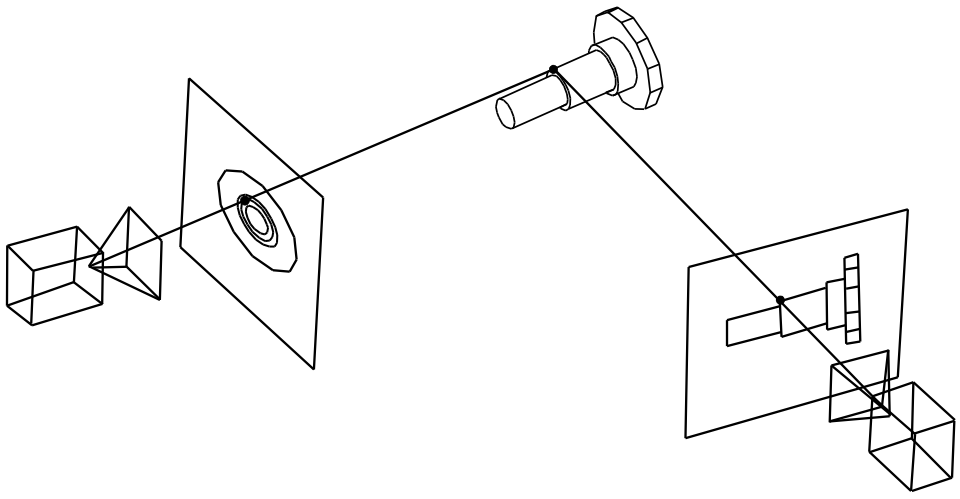

Figure 10. *Illustration of imaging an object from two views. The 3D point is shown as an intersection of the rays connecting the corresponding image point with the camera center.*

Once the camera matrices $\widetilde{\mathbf{P}}$ and $\widetilde{\mathbf{P}}'$ and the point correspondences $\widetilde{\mathbf{m}}_i \leftrightarrow \widetilde{\mathbf{m}}'_i$ between the images are known, the 3D points $\widetilde{\mathbf{M}}_i$ can be solved from the equation pair arising from the basic equation (3):

$$\begin{cases} \widetilde{\mathbf{m}}_i = \mathbf{P}\widetilde{\mathbf{M}}_i \\ \widetilde{\mathbf{m}}'_i = \mathbf{P}'\widetilde{\mathbf{M}}_i \end{cases}. \tag{28}$$

Applying (22) to (28) and rearranging yields the following equation

$$\begin{bmatrix} u_i\mathbf{p}^3 - \mathbf{p}^1 \\ v_i\mathbf{p}^3 - \mathbf{p}^2 \\ u'_i\,\mathbf{p}'^3 - \mathbf{p}'^1 \\ v'_i\,\mathbf{p}'^3 - \mathbf{p}'^2 \end{bmatrix} \mathbf{M}_i = \mathbf{0}, \tag{29}$$

which can be solved with SVD similarly to (22). (Hartley & Zisserman 2004, pp. 312-313).

Finding the correspondences $\widetilde{\mathbf{m}}_i \leftrightarrow \widetilde{\mathbf{m}}'_i$ required in solving (28) is the most challenging phase of the 3D reconstruction (Moons et al. 2009). Commonly, the image features such as corners, edges or regions of interest points are first detected using sufficient feature detectors and then local descriptors are computed for each region around the features (Zakharov 2015). The descriptors act as the fingerprints of the regions and they are used in finding the corresponding regions. If the conditions of the imaged area are regulated as the case in laboratory conditions often is and the objects of interest have known morphologies, the image features as such can be used in finding the correspondences. Also, if the camera poses are known exactly and the objects of interest have a simple geometry, the locations in the images can be used as the correspondences (Kwon et al. 2013).

3.7 Morphological Thinning

Morphological thinning is an operation where a binary object is reduced to a one-pixel-wide centerline approximation that is termed skeleton. The skeletons reduce the data needed for presenting the object and they enable simpler structural analysis and more intuitive design of recognition algorithms (Lam et al. 1992). Skeletons are a powerful way of presenting the fiber geometry as already mentioned in Section 2.4.2. Thinning is a fundamental preprocessing technique, and a wide range of thinning methods exists in the literature. The methods can be classified to iterative and non-iterative and the non-iterative methods can be further divided into sequential and parallel methods (Saeed et al. 2010). The appropriate thinning methods should be chosen based on the application. A broad

survey of thinning algorithms is given in (Lam et al. 1992) and a more recent review is presented in (Saeed et al. 2010).

p_1	p_2	p_3
p_8	p	p_4
p_7	p_6	p_5

Figure 11. *The 3 x 3 neighborhood of the pixel* p*.*

The method suggested by (Guo & Hall 1989) is used in this thesis work as it preserves the fiber topology and is fast enough for online applications. The algorithm is a parallel two-subiteration algorithm. It checks the 3 x 3 neighborhood of the pixel (see Figure 11) and removes the pixel if the following conditions of its neighboring pixels are true:

1. $C(p) = 1$
2. $2 \leq N(p) \leq 3$
3. $(p_2 \vee p_3 \vee \overline{p}_5) \wedge p_4 = 0$, odd iterations

   $(p_6 \vee p_7 \vee \overline{p}_1) \wedge p_8 = 0$, even iterations.

C(p) is the number of distinct 8-connected components in *p*'s neighborhood ($p_1 \ldots p_8$) and *N(p)* is defined as follows:

$$N(p) = \min(N_1(p), N_2(p)), \tag{30}$$

where

$$N_1(p) = (p_1 \vee p_2) + (p_3 \vee p_4) + (p_5 \vee p_6) + (p_7 \vee p_8) \tag{31}$$

$$N_2(p) = (p_2 \vee p_3) + (p_4 \vee p_5) + (p_6 \vee p_7) + (p_8 \vee p_1). \quad (32)$$

Thinning proceeds by removing in distinct iterations first north and east, and then south and west boundary pixel of the object. The algorithm is applied iteratively until no further thinning is possible.

3.8 Pruning

Thinning methods often produce erroneous spurs i.e. short arcs that are not important part of the skeleton. The spurs are caused by roughness and irregularities in the boundary of the binary object. The spurs have to be removed since they cause errors in the analysis of the skeleton. The pruning algorithm described in (Niemistö et al. 2005) is applied in this thesis work. It is an iterative algorithm consisting of four steps. As a prerequisite, the maximum spur length in pixels N_p has to be defined. The steps of the algorithm are the following (Niemistö et al. 2005):

1. Remove all pixels in the 3 x 3 neighborhoods of the branch points from the skeleton image *S* and store the result in *K*.

2. Remove all 8-connected components from *K* without an end point of an 8-connected component in *S* and store the result in *K*.

3. Remove all pixels from *S* that correspond to an 8-connected component in *K* consisting of less than or equal to N_p –1 pixels, and store the result in *S*.

4. Remove all pixels from *S* that are end point in the 3 x 3 neighborhood of a branch point and store the results in *S*.

These steps are executed until no change occurs in the image between two iterations. This way, also the spurs with spurs are removed. The pruning process is illustrated in Figure 12.

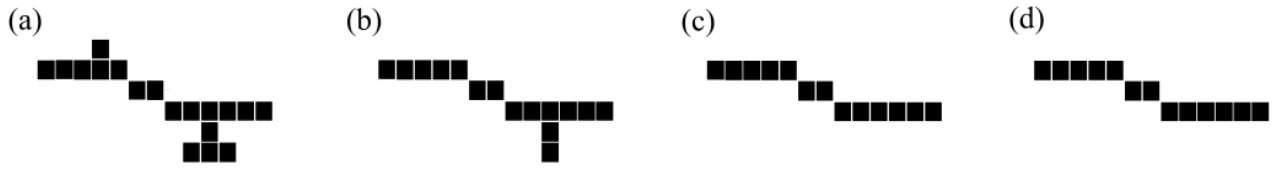

Figure 12. *Pruning process with N_p = 2. Original skeleton (a), after the first iteration (b), after the second iteration (c), and after the third iteration (d). There is no change in the skeleton between (c) and (d) and thus the algorithm stops.*

4 Experiments and Results

This chapter discusses the experiments performed and the results gained in this thesis work. The chapter is divided into seven sections: six of them are each presenting an element required in answering to the research questions defined in Section 1.2, and the seventh gives a performance evaluation. Section 4.1 discusses fiber detection, which is a prerequisite for any other task of the thesis. The section describes the solutions in illumination of fibers and in segmentation of images. Section 4.2 presents the computer vision algorithm developed for inspecting the wet fibers placed on the microrobotic platform. The algorithm consists of ensuring that the fiber is graspable with the platform and that it fulfils the user's requirements. Section 4.3 discusses the calibration of the vision system of Fibrobot II for 3D measurements that are needed for automated grasping of dry fibers and dry fiber bonds. The algorithm for 3D reconstruction of individual dry fibers is presented in Section 4.4. The algorithm and the reference measurements and data analysis to validate it are described. Section 4.5 discusses extending the 3D reconstruction method for individual fiber bonds. Section 4.6 presents the algorithms to find suitable grasp points from the 2D geometries representing wet fibers and the reconstructed 3D geometries representing dry fiber bonds. The same algorithms with minor modifications suit the dry fibers as well. Finally, Section 4.7 offers a brief evaluation of the performance of the algorithms. All the algorithms were implemented in Python using the modules OpenCV, Numpy and Scipy (Oliphant 2007).

4.1 Fiber Detection

Proper illumination is crucial for micromanipulation tasks under an optical microscope. Illumination has to be adjusted based on the properties and the shape of the parts to be manipulated and the platform to be used. (Probst et al. 2009). The illumination solutions found in the literature and presented in Section 2.4.1 were designed for rigid parts and rather small field of views, and they did not suit the fiber studies on our microrobotic platforms. Therefore, a new illumination system was built to enhance the contrast between the background and the fibers. A high contrast enables the use of simple and efficient preprocessing methods such as thresholding in segmentation. Publication I presents the design and implementation of the illumination system. The design process had three steps. First, the most prominent illumination techniques for this particular problem were searched from the literature. Polarized light, ring light and dark field illumination were chosen based on the similarity of the applications, in which they had been used, and the theoretical suitability. Second, prototypes of the three chosen techniques were built and tested with paper fibers samples and with the camera and the optics of the Fibrobot I platform. Ten images of approximately 300 wet paper fibers in total were taken with each prototype. The comparison was done by using two thresholding techniques

and counting manually the number of fiber objects missing from the binary image and the number of fiber objects with clear breakages and shortenings in the binary image. Finally, the best-functioning illumination system was integrated into the sample stage of the platform. The final illumination system utilized polarized light and it was used in the experiments reported in Publications II, IV and V. Figure 13 shows a comparison between an image taken with the coaxial bright light illumination integrated in the optics of Fibrobot I and the designed illumination system. The contrast between the fibers and the background is superb with the designed system as it can be seen in the figure.

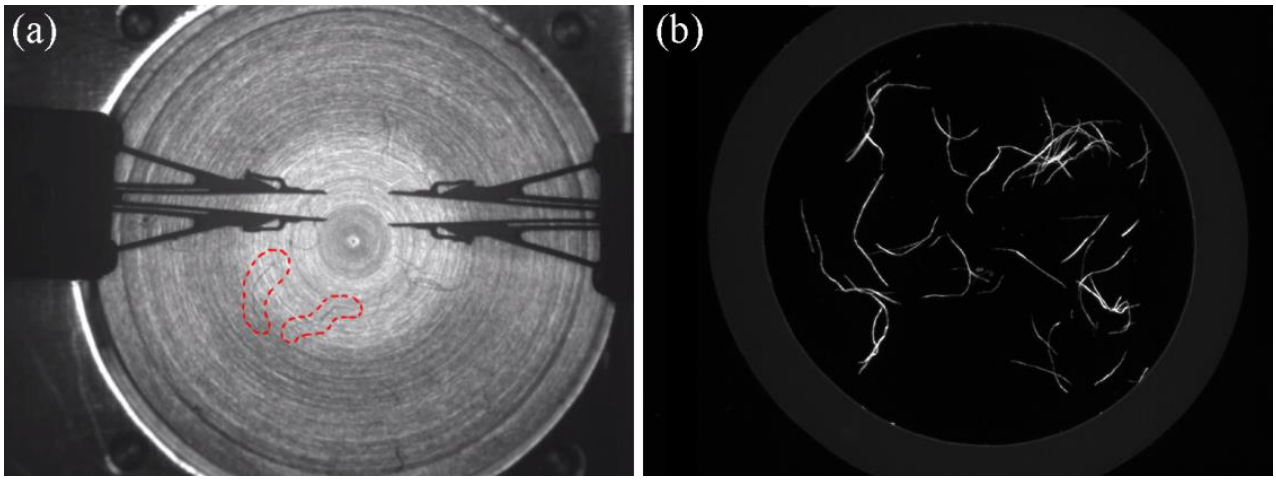

Figure 13. *An image taken of paper fibers on the platform with coaxial bright light illumination (a) and with the designed illumination system (b). Two fibers are encircled with red dashed line in (a) to enhance visibility.*

The performance of the designed illumination system was assessed by taking multiple images of high number of random fibers, converting the images to binary images, and manually counting the numbers of the missing and the broken fiber objects from the binary images. This gives two ratios: a detection ratio that describes the ratio between the number of the fiber objects in the binary images and the number of the imaged fibers, and a breakage ratio that defines the ratio between the fiber objects with breakages or shortenings in the binary images and the number of the fiber objects in the binary images. Table III shows the performance of the designed illumination system.

Table III: *Performance of the developed illumination system*

Detection ratio	*Breakage ratio*	*Total number of fibers*
0.99	0.10	258

The implemented illumination system is based on polarized backlight and it utilizes the polarizing properties of paper fibers, mainly the S_2-layer (see Figure 1, page 17). The sample holder is made of glass, and the light source, the diffuser and the polarizer lie below the sample holder. They are fixed on a rod going through the hollow shaft of the rotary stage. This way the light source, the diffuser and the polarizer remain static while the rotary stage rotates. The motion of the rotary stage is transmitted to the sample holder by a cylinder that surrounds the rod. There is another polarizer with 90˚ angle to the first polarizer attached to the optics of the camera. The light that does not pass through any fiber is blocked by the second polarizer due to the angle difference of the polarizers. However, the light that passes through the fiber samples changes its polarity and travels to the camera through the second polarizer. Therefore, the bright fiber objects are seen on the black background in the images when the illumination system is used.

As the contrast between the fibers and the background is high in the images, thresholding is used to distinguish the fibers from the background in the experiments reported in Publications II, IV and V. Fixed threshold is used in Publication II. A binary image *b(u, v)* is constructed of an 8-bit grayscale image *f(u, v)* by using a certain threshold $T \in [0, 255]$ as follows

$$b(u,v) = \begin{cases} 0, & f(u,v) < T \\ 1, & f(u,v) \geq T \end{cases} \tag{33}$$

The threshold is set to a value, which gives a good result with the used exposure time and the input power of the illumination system, and these parameters are maintained constant during the test. Due to the differences in the polarizing properties of the fibers, there are changes in the brightness between the fibers in the grayscale image. Therefore, getting intact fiber objects in the binary image requires quite a low threshold. This produces sometimes dilated fiber objects of the fibers that are seen brighter in the image. Figure 14 illustrates this.

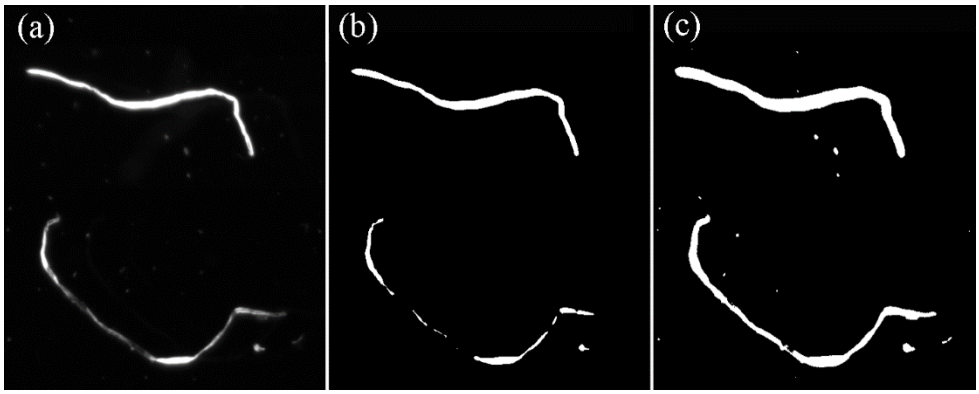

Figure 14. *Challenges of the change in fiber brightness to the global threshold. Original image (a), a binary image where the upper fiber is morphologically well preserved but the lower fiber has breakages (T = 104) (b), and a binary image where the lower fiber is intact but the upper fiber is dilated (T = 35) (c).*

A bit modified iterative thresholding procedure was utilized in Publications IV and V to overcome this. The procedure used two thresholds T_{low} and T_{high} and a step ΔT and it had three steps:

1. Generate binary images $b_{low}(u, v)$ and $b_{high}(u, v)$ by using the T_{low} and T_{high} similarly to (33).
2. Define $b(u, v) = b_{low}(u, v)$ *AND* $b_{high}(u, v)$.
3. If there is only one binary object in $b(u, v)$, it is the final result. Else, set $T_{high} = T_{high} - \Delta T$ and go back to Step 1.

There was only one fiber object imaged at time in the experiments of Publications IV and V. If there are multiple fiber objects in the image, the steps have to be performed individually for each binary object after conducting Step 1 for the first time. The iterative procedure ensures that the highest threshold to produce intact binary object of a fiber is used.

4.2 Wet Fiber Inspection

Publication II discusses analyzing images of wet fibers for automated grasping. There is a need for measuring wet and dry fibers, as Section 2.3 described, and the type of the samples affects the design of the algorithms. Wet fibers remain immersed in the thin layer of water in the well of the

sample stage and hence they can be estimated to stay on a plane. Therefore, 2D analysis is sufficient and only one camera on top of the platform is needed. Fibrobot I was used in the experiments of the paper. The novelty of the paper was to formulate rules for grasping fiber-like flexible 2D objects with microgrippers.

After detecting the fibers from the image as described in the previous section, the next step is to inspect if it is possible to grasp the fibers with the microgrippers of the platform. A graspable fiber should be long enough to enable secure grasping, should not overlap with any other fiber, and should be straight enough for grasping as the XYZ micropositioners that move the grippers do not have rotational axes. Also, the proximity of the grasping points should be free of obstacles to ensure that the grippers do not hit anything and grasp only the target fiber. The inspection was based on the morphology of the fiber skeletons. The fiber skeletons were extracted from the binary image with the morphological thinning method by (Guo & Hall 1989), and the erroneous spurs were removed with a pruning method by (Niemistö et al. 2005). The same thinning and pruning methods were used also in Publications IV and V. The result is a one-pixel wide approximation of the fiber centerline. The rules for valid grasp points were formed by utilizing the experience of a human operator, who had conducted fiber manipulation experiments with the platform in tele-operated mode for six years. The grasp point detection is presented in Section 4.6.

The performance of the algorithm was compared with the performance of the human operator by using four sets of 15 images of 189 fiber objects in total. The comparison involved classification of the fibers to graspable and non-graspable, and the suggested grasping points. The algorithm proved to be considerably faster and much more consistent with its choices. The average execution times per image for the human and the algorithm were 18.4 s and 4.2 s, respectively. When the image of the same scene was shown in four different orientations, only around 50% of the chosen fibers by the human operator were chosen in all the orientations whereas the corresponding percentage was over 90% in the case of the algorithm. Also, the distance between the grasping points chosen by the algorithm for the different orientations was only half of that for human. The sensitivity and the specificity of the algorithm were calculated by using the human choices as the ground truth, and the results were 0.83 and 0.92, respectively. This indicates that the algorithm mimicked human choices well although the low consistency of the human choices affects the results.

4.3 Calibration

The dry fibers and dry fiber bonds used in the experiments in Publications IV and V are true 3D objects with random geometries. Therefore, 3D reconstruction is required in inspecting their geometry for grasping and detecting suitable grasping points. The camera – microrobot system calibration

methods presented in Section 3.4.1 were all based on modeling the camera as a pure plane transformation. Thus, the 3D reconstruction is possible in the case of two cameras only at the intersection line of the object planes. Basic pinhole camera model (Section 3.4) and the DLT calibration method described in Section 3.5.1 were used for camera calibration in Publications III, IV and V.

Publication III presents the calibration process and the experiments to validate that the process is precise enough for microrobotic grasping performed with the platform. Publication III also presents the method to track the tip of the gripper actuator by attaching a cheap and easily fabricated planar dot grid pattern on it (Figure 4c, page 39). The pattern was fabricated in a normal darkroom by exposing a photographic paper under a photolithography mask and using standard film developing chemicals. The benefit of the planar pattern compared with e.g. template matching is that the orientation and the scale of the actuator do not affect the detection as long as the pattern is visible. This is advantageous especially in prototyping environments, where the platform composition or even the camera angles do not remain static between the tests. Also, the microgripper jaws are not straightforward to find from the image due to their bulky shape and the challenging camera angles. Furthermore, the most interesting point to track is the lower corner of the gripper tip, and it is not usually visible in the images. The experiments presented in Publication III include tracking the gripper actuator, reconstructing a physical 3D reference object and performing true grasping experiments. It was shown that the same calibration and gripper jaw tracking procedure was valid for different gripper angles and camera poses. Also, the precision of the 3D reconstruction performed with the camera matrices produced with the proposed calibration procedure was comparable with the result obtained using the camera matrices generated by utilizing a commercial planar calibration pattern and the calibration procedure of OpenCV. The dot grid patterns used in Publications IV and V were considerably smaller than the first prototypes reported in Publication III.

As the purpose of the camera matrices was bare 3D reconstruction, no actual intrinsic or extrinsic camera parameters were solved and the final results were 3 x 4 matrices with numerical values. For example, one of the camera matrices used for 3D reconstruction in Publication V was as follows

$$\mathbf{P} = \begin{bmatrix} 0.167 & 0.016 & 0.042 & 1177.730 \\ 0.016 & -0.172 & 0.001 & 951.458 \\ 0 & 0 & 0 & 1 \end{bmatrix} \tag{34}$$

Fibrobot I with an external camera on a tripod was used in Publication III and Fibrobot II was used in the Publications IV and V. The image point – 3D point correspondences were acquired by utilizing the XYZ micropositioners of the microgrippers of the platform. The microgrippers were moved in several different positions in the field and the depth of view of the cameras, and images were captured in each position. The image points were acquired by tracking the pattern in the images and the

3D points were read from the position sensors of the micropositioners. Figure 15 presents the calibration procedure.

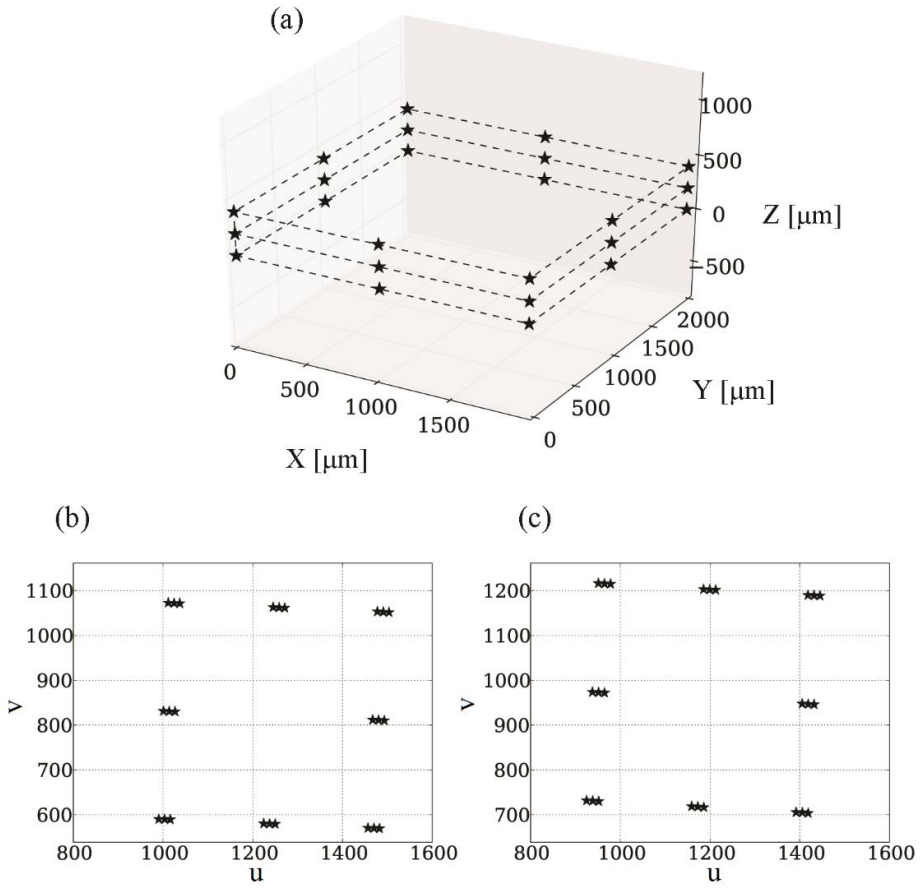

Figure 15. *The calibration procedure. The 3D trajectory of the microgripper from the position sensors of the micropositioners (a), the location of the center of the upper left dot of the pattern attached to the gripper in the view of camera 1 (b) and camera 2 (c).*

The solved camera matrices link an image point correspondence between the two views to the corresponding 3D point in the frame of the manipulator that was used in the calibration. This is convenient for automated manipulation. By utilizing the method described in Publication III, the offset between the planar marker and the gripper tip can be solved by utilizing a reference measurement and a plane transformation. The camera matrices have to be solved for each of the manipulators that are needed in the manipulation task since their frames are different as shown in Figure 9 (page 48).

The modern microscope objectives are corrected for most common optical artefacts including radial distortions. Hence, the radial distortion coefficients are weak as pointed out by (Tamadazte et al. 2008) and reported by (Zhou & Nelson 1999). Accordingly, most of the studies presented in Section 2.4.1 ignore radial distortion (Wang et al. 2010; Wason et al. 2012; Xing et al. 2014; Das et al. 2012; Tamadazte et al. 2010; Jasper et al. 2011). According to the tests done with Fibrobot II, the radial distortion coefficients k_1 and k_2 of the optics were in the scales of 10^{-10} and 10^{-15} or less, respectively. Therefore, the effect of the radial distortion was negligible and there was no need to consider it in calibration or imaging in general.

The quality of the camera matrices calculated was assessed by computing the reprojection error and the metric position error from the grid positions in a cuboidal trajectory consisting of 144 points outside the calibration trajectory. The reprojection errors were around 0.2 – 0.3 pixels and the average position error was less than 2.5 µm for Fibrobot II. This indicates that the precision was adequate for the grasping tasks. The position error was slightly higher (3.0 µm) for Fibrobot I in Publication III due to different optics, larger field of view and larger calibration trajectory.

4.4 Fiber 3D Reconstruction

Publication IV presents a method for fiber 3D reconstruction on Fibrobot II. The changes of curvature in the fiber skeletons were utilized as the image point correspondences between the two camera views. The camera matrices needed in the reconstruction were acquired by using the calibration procedure described in Section 4.3. The novelties of the paper were presenting rules to avoid and remove mismatches in the correspondences, reconstructing the 3D geometry of an irregular object on a microrobotic platform, and comparing the reconstructed geometry with a reference measurement with the µCT. The mismatch avoidance consisted of two steps. First, the curvature change points with a difference less than a certain threshold from the preceding or following change point were omitted from the data of both views. Then, the data were cross-correlated and the nearest change points with the same direction were paired.

The fibers were casted in PDMS to hold them still between imaging with the microrobotic platform and the µCT. Four samples were imaged in 16 different orientations on the platform by utilizing the rotary stage. Figure 16 shows an image of one of the fiber samples taken with FibRobot II. The overall mismatch rate was as low as 2% and only 13% of the reconstructions had at least one mismatch. Most of the mismatches did not have a big effect on the reconstruction. The reconstructed geometries were evaluated by comparing the results from 16 different orientations with each other and with the µCT reference. The first comparison gave the variance of the reconstructions, and the comparison with µCT images yielded the deviation from the reference. To perform the comparisons, the reconstructions from the different orientations were first aligned with each other by utilizing the

data from the position sensor of the rotary stage. For the comparison with µCT, each reconstruction was then aligned with the reference by applying the iterative closest point (ICP) algorithm (Besl & McKay 1992). The average point-to-point distance between the reconstructed and the reference fiber skeletons was 20 – 30 µm, which was around half of the fiber diameter. This shows that the reconstructed 3D geometry mostly followed the fiber borders, and the method is applicable to automated fiber handling. The average point-to-point distance between the aligned reconstructions was also 20 – 30 µm although the maximum distances were higher. This shows that the bundle of reconstructions is scattered around the reference and the greatest difference is between the reconstructions that have the errors to the opposite directions. Table IV shows the average and maximum point-to-point distances between the different orientations and between each of the orientations and the reference. Figure 17 shows the comparison between the 3D reconstructions of the fiber sample in Figure 16 and its µCT reference.

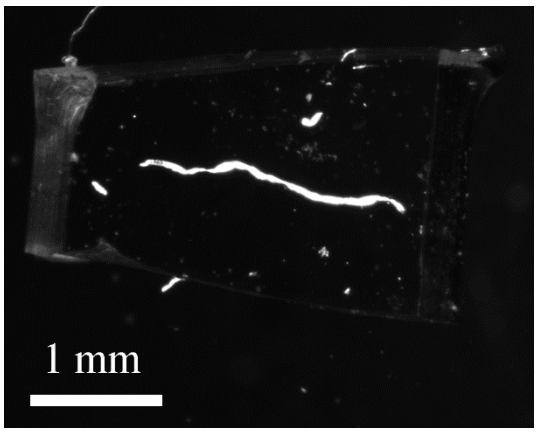

Figure 16. *A fiber sample casted in PDMS.*

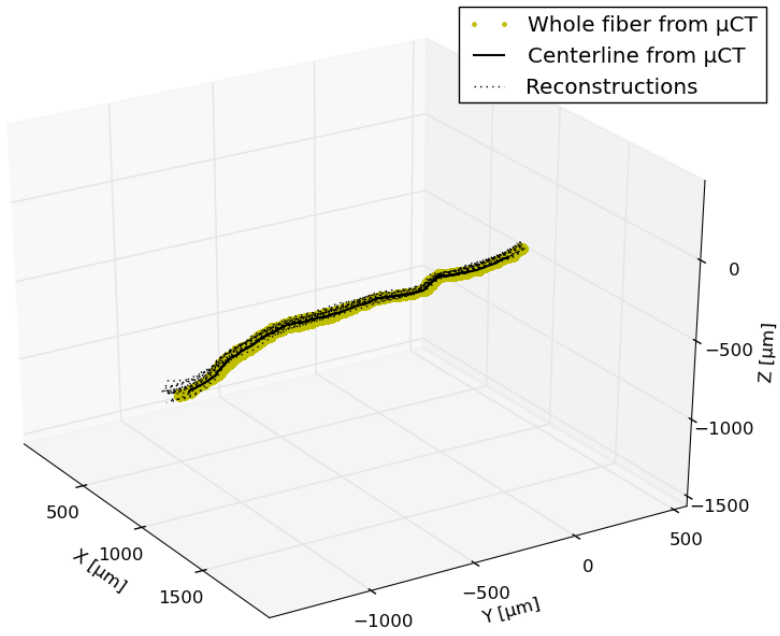

Figure 17. *The 16 3D reconstructions of one of the samples aligned with each other and the µCT reference.*

Table IV. *Point-to-point distances between the aligned reconstructions, and point-to-point distances between each reconstruction and the µCT reference*.

Sample	*Distance from each other (µm)*		*Distance from the µCT reference (µm)*	
	Mean	*Max*	*Mean*	*Max*
I	23 ± 13	113	24 ± 8	44 ± 10
II	22 ± 17	183	28 ± 7	64 ± 34
III	28 ± 22	152	22 ± 10	56 ± 18
IV	24 ± 19	153	22 ± 9	51 ± 22

In addition, the sensitivity of the method to the orientation of the sample, and the noise sensitivity were addressed in Publication IV. The suitability for automated fiber handling was also demonstrated in (Essen et al. 2014) where the 3D reconstruction method and a 3D extension of the grasping rules presented in Publication II were used in automated fiber grasping experiments. 70 fibers were grasped and lifted from the sample stage with a success rate of 79%. Less than half of the failures were caused by the errors in the 3D reconstruction, which raises the success rate of the method to 90%.

4.5 Bond 3D Reconstruction

Publication V presents the algorithms to extend the fiber 3D reconstruction method of Publication IV to be applicable to fiber bonds. It describes a strategy to validate that the skeleton describes a legal bond consisting of two fibers, and an approach to separate the skeleton to two fiber skeletons. The legal bond skeleton should have four end points and one or two branch points, as the branches do not necessary continue from the same pixel that the opposite branch ends to. However, the distance between the branch points should not exceed the estimated maximum width of the fiber. The end points and the branch points were detected by using a hit-and-miss algorithm and appropriate structuring elements. After ensuring that the skeleton is legal, the bond branches of both views were sorted in clockwise order to pair the branches belonging to the same fiber skeleton together. Then, the fiber skeletons were paired between the views by using the k-nearest neighbors algorithm. The 3D reconstructions of the paired fiber skeletons were built by using the method described in Publication IV. Publication V also presents a method to find suitable grasp points from the reconstructed 3D bond skeleton. The novelties of the publication are reconstructing a 3D model of a fiber bond placed on a microrobotic platform, and formulating mathematical rules for detecting sufficient grasp points from the reconstruction. Figure 18 presents the steps of the bond 3D reconstruction and the grasp point detection algorithm.

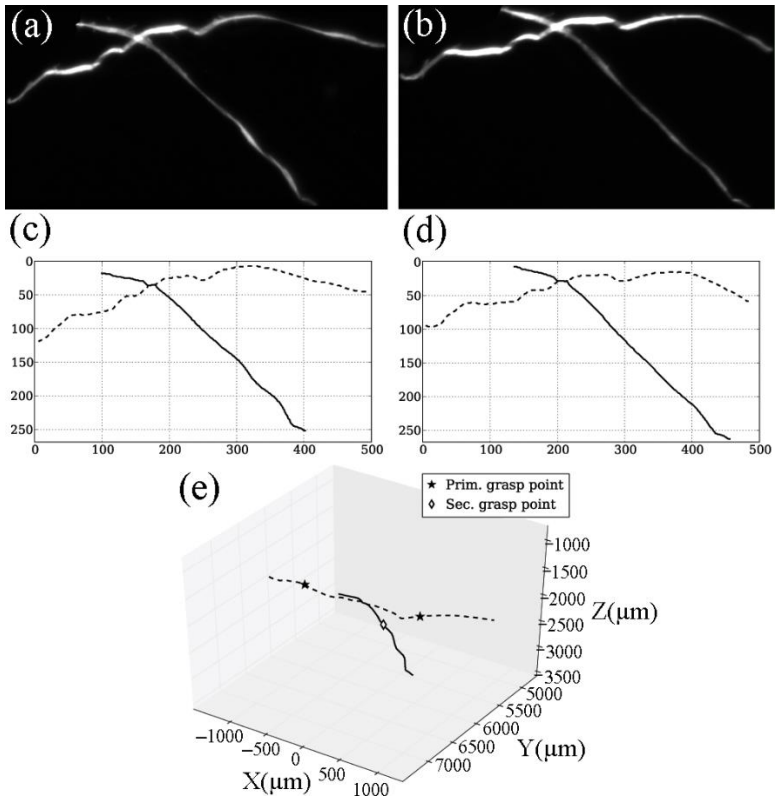

Figure 18. *Steps of the bond 3D reconstruction and grasp point detection algorithm. Original images (a, b), paired fiber skeletons (c, d), and the 3D skeleton with the calculated grasp points (e).*

Both the reconstruction and the grasp point detection method were validated by real manipulation experiments, where the fiber bonds were grasped with three grippers as shown in Figure 2f (page 22) and pulled apart. Seven fiber bonds were tested. Two bonds were classified as ungraspable, grasping and pulling succeeded with four bonds and failed with one bond. This gives the success rate with the graspable fiber bonds 80%, which is generally quite high for demanding micromanipulation tasks.

4.6 Grasp Point Detection

Publication II presents the grasp point detection algorithm for fibers and Publication V describes the grasp point detection algorithm for bonds. The algorithm presented in Publication II is designed for wet fibers that stay planar on the sample stage, but it is applicable to dry fibers that are truly 3D

objects with minor modifications. The four conditions for the grasp point for the wet fiber are illustrated in Figure 19 and they are defined as follows:

1. The angles between the line that connects the grasp points to each other and the lines that connect the grasp point to the end points of its section should be ≥ θ_{min} (the outer section end point) and ≤ 180°– θ_{min} (the inner section end point). The gripper geometry defines the section length e_{min}.

2. The ending of the fiber should not be folded double on the grasping point. Thus, a line connecting the grasp points and the lines connecting the grasp points to the nearest fiber end points should have angle > 90°.

3. The length of the fiber section between the grasping points L' should exceed the minimum length l_{min} required for the further experiments.

4. The length of the endings e_1, e_2 should be in a given range [e_{min}, e_{max}].

The rules 1 and 2 are grasping fundamentals and the rules 3 and 4 are defined by the user according to the experiments to be done.

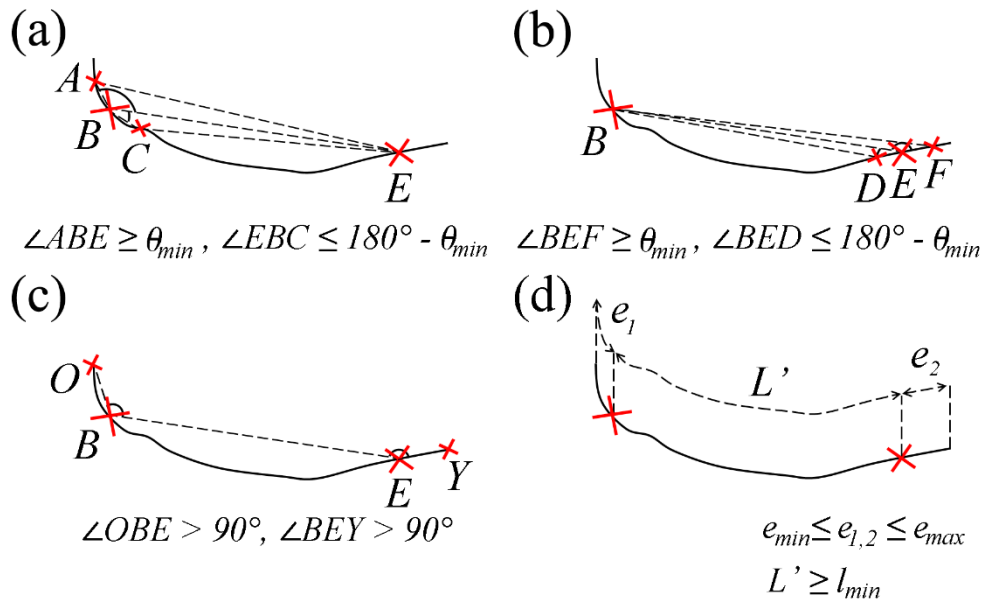

Figure 19. *The grasping rules for a wet fiber. Straightness constraints (a, b, c) and length constraints (d). Points A and F are the outer section end points and points C and D are the inner section end points.*

The grasp points detected by the human and the algorithm were compared with each other in Publication II. When the same scene was shown in four different orientations, the distance between the grasp points that the human chose for the same fiber end was double compared with the choices of the algorithm (130 µm vs. 65 µm). The average distance between the grasp points chosen by the human and the grasp points chosen by the algorithm was 220 µm. Figure 20 shows the comparison of the grasp points selected by the human and the algorithm.

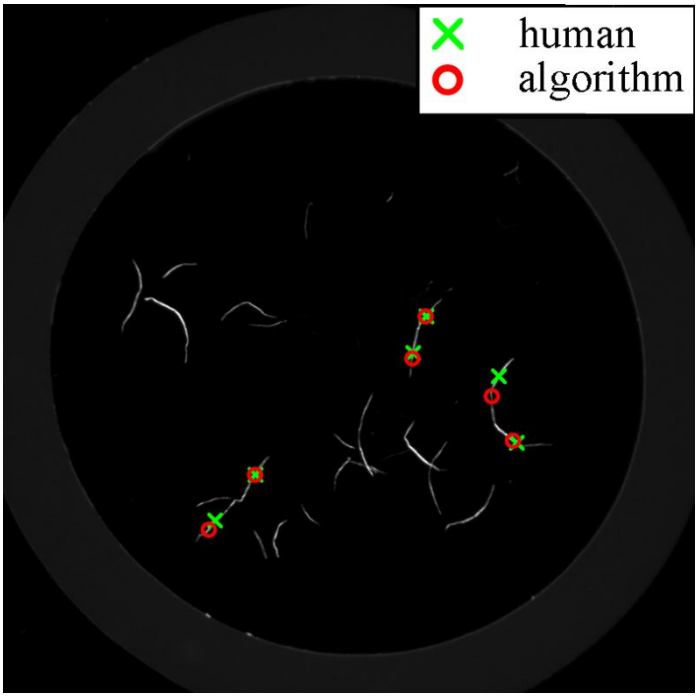

Figure 20. *The grasp points selected by the human and the algorithm plotted on the same picture.*

In the case of a bond, the grasp points were divided into the primary points and the secondary point denoting the fiber that is grasped. The five conditions for the grasp points for a bond are

1. Distance between the center of the bond and the grasp points should be minimal
2. Yet, the distance between the primary grasp points and the bond center should exceed a set minimum to prevent grasping the bond itself, and the distance between the secondary grasp point and the bond center should exceed another set minimum to prevent the grippers from clashing with each other.

3. The distance between the grasp point and the adjacent fiber should exceed a set minimum for the gripper jaws to fit between the fibers.

4. The fiber sections between the grasp point and the end point of the same bond branch should exceed a set minimum to ensure a firm grasp.

5. The fiber sections should be straight enough. Primary points should fulfill Condition 1 for the grasp point for a fiber (page 68), and the fiber section close to the secondary point should be parallel to the line that is perpendicular to the line that joins the primary points.

Figure 21 presents the conditions.

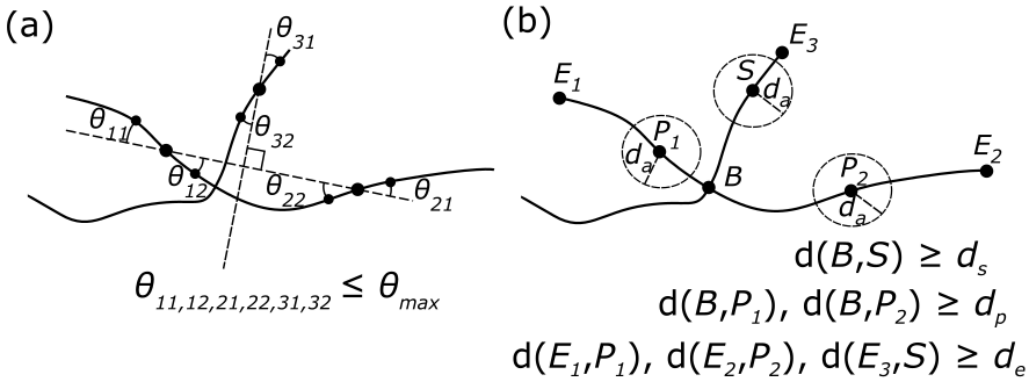

Figure 21. *The straightness conditions (a) and the spatial conditions (b) for the grasp points on the fiber bond*

After detecting the grasp points, the fiber or the fiber bond needs to be aligned with the grippers in order to grasp it. In the case of fibers, this means simply calculating the angle between the line that connects the grasp points in the XY plane and the common Y axis of the north and south gripper (Fibrobot II), and turning the rotary stage to compensate that angle. In the case of bonds, it is furthermore required to ensure that the secondary grasp point will be on the same side of the bond with the west gripper after the rotation. Thus, after calculating the angle needed for aligning the primary grasp points with the north and south grippers as described above, the XY coordinates of all the grasp points after such rotation are calculated and inspected. If the calculated secondary grasp point is on the right side on the bond (the west gripper is on the left side), the correct angle for the rotary stage will have the magnitude of the supplementary angle of the original angle and the opposite direction, as clarified in Figure 22. After the alignment, new images are taken and the grasp points are recalculated.

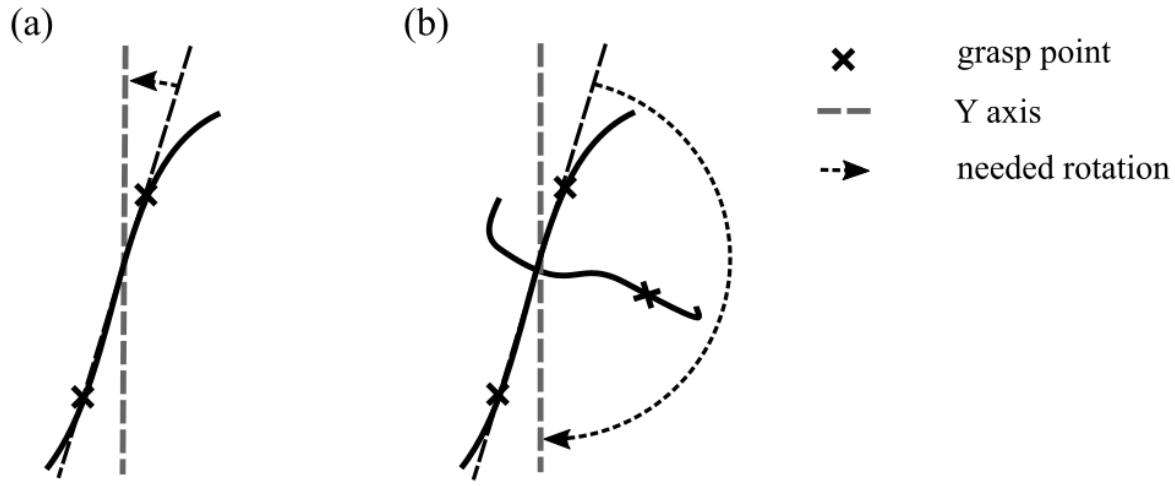

Figure 22. *Aligning a fiber (a) and a fiber bond (b) with the microgrippers.*

In the case of the 3D coordinates, the grasp points must be next transformed to the frames of the corresponding microgrippers. Regarding bonds, the upper primary grasp point has to be in the frame of the north gripper, the lower primary grasp point in the frame of the south gripper and the secondary grasp point in the frame of the west gripper. The 3D reconstruction is calculated by using the camera matrices produced by utilizing one of the microgrippers, and hence all the grasp points are in the frame of that microgripper. The frame transformation requires first reprojecting the 3D grasp point to the image point pair in the image planes of the cameras, and then applying (28) and the camera matrices of the corresponding microgripper to solve the 3D grasp point in its frame.

Automated grasp point detection, alignment and grasping was performed in Publication V. There, seven different fiber bonds were individually placed on the rotary stage and attempted to be grasped and pulled apart. Grasp points fulfilling the conditions were not found from two of the fiber bonds. From the five fiber bonds with legal grasp points, the grasping and pulling succeeded with four and failed with one. The cause for the failure was slipping of the secondary fiber from between of the gripper jaws. Table V presents the parameters used in the grasping test.

Table V: *Parameter for the grasping test.*

Parameter name	*Value*
Image processing parameters	
Threshold for binarization	30
Maximum diameter of the trash particles	100 pix
Maximum fiber width	50 µm
Grasp point constraints (the symbol in Figure 21 in brackets)	
Maximum angle in grasping section (θ_{max})	30˚
Grasping section length	200 µm
Primary point – bonding point distance (d_p)	100 µm
Secondary point – bonding point distance (d_s)	350 µm
Grasp point – end point distance (d_e)	100 µm
Grasp point – adjacent fiber distance (d_a)	500 µm

4.7 Performance Evaluation

The optimal condition for the illumination system is dark ambient. However, the experiments in Publication V and some not-published demos were performed in ambient room light and its disturbance was negligible. The iterative thresholding method used in producing the binary images ensures that the lowest possible threshold for each fiber is always used and thus minimizes the dilation of the binary fiber objects but does not fully solve the problem. There are darker and brighter sections in each fiber, and using the same threshold for the whole fiber can cause thickening of the brighter sections if the difference in brightness between the sections is significant. However, the tests have proven that the morphology remains nevertheless sufficient for 3D reconstruction. Also, the changes in brightness may offer useful information of structure defects of the fibers.

The threshold values depend on the exposure of the cameras and the zoom level of the optics. Optimal threshold has to be experimentally found for each of the zoom levels needed in the experiments. The maximum diameter of the binary objects that were interpreted as trash particles and the spur length for pruning were defined in pixels in Publications IV and V. These values work only to the specific zoom levels used in those experiments. However, the range of the spatial resolution for the optics is given by the manufacturer and hence solving the parameters for each zoom level is straightforward.

The preprocessing parameters related to fiber dimensions and some of the reconstruction parameters applied in calculation of the curvature and detecting the curvature points are sensitive to the fiber types used. Using fibers from different wood and plant types requires tuning of the parameters. The parameters related to fiber dimensions are found in literature but modifying the others needs experimental work.

The parameters needed in grasp point search such as the minimum and the maximum lengths of different fiber sections and fiber angles near the grasp point depend on the gripper type used. The thickness of the gripper jaws, their shape and their maximum opening define the geometries that are possible to be firmly grasped with the grippers. The grasp point search parameters presented in the papers were experimentally found to be functional. Regarding the wet fibers, the proportion of the fibers classified as graspable was in line with the results of the human operator. However, in the case of the bonds, similar comparison was not made. Thus, it may be possible to further optimize the parameters to increase the proportion. On the contrary, the success rate of the experiments reported in Publication V was 80%, and this suggests that the proportion was even too high. As a conclusion, the tighter the grasp point constraints, the lower the proportion of the fibers and bonds classified as graspable and the lower the failure rate.

The speed of the developed algorithms outperforms tele-operated tasks. The detection and inspection algorithm of wet fibers executed in 4.2 seconds on average, which is remarkably less than the average of 18.4 seconds required for the experienced human operator. The 3D reconstruction of individual fiber took 2.3 seconds on average and automated grasping and breaking a fiber bond required 10 – 15 seconds. As the comparison, tele-operated fiber manipulation tasks typically take several minutes (Saketi et al. 2012). Nevertheless, the execution times of the algorithms can and should be further decreased by translating them to some more computationally efficient programming language such as C++ and implementing the iterative parts with e.g. tree structures instead of computationally heavy loops. The further acceleration would make the automation smoother and significantly raise the yield.

5 Conclusions

This chapter is divided into three sections. The first section summarizes the results of this thesis work. The second section returns to the research questions defined in Section 1.2 and provides answers to them based on the results of the thesis. The final section discusses possible future work and concludes the thesis.

5.1 Summary of the Results

This thesis has presented illumination and computer vision solutions for automated fiber manipulation on a micro robotic platform. The experiments carried out for this study prove that the illumination system and the algorithms are reliable and repeatable, and that they do indeed enable the automated grasping of wet and dry paper fibers and dry paper fiber bonds.

The illumination system developed here exploits the polarizing properties of the fibers to produce high-contrast images, and hence it is applicable for any polarizing material. It enables the detection of thin transparent samples, which are extremely challenging with conventional illumination systems. This is the first time such an illumination solution has been presented with a micro robotic system. The main drawback with this lighting system is that any actuators on a platform using this illumination system need to be made of polarizing material in order to be visible in the image. However, the grasping experiments performed for this work showed that if the actuators are calibrated before the tests, there is no need for them to be visible. Alternatively, it has been reported in the literature that a different illumination system can be used for viewing the actuators.

The algorithm for 2D fiber detection, assessing the fiber's graspability and detecting the optimal grasp points compared well with human decision-making and outperformed human performance in terms of repeatability and consistency. The algorithm can be applied to any type of fibers as long as the samples are planar. Although an innovative illumination system was developed for these experiments, any illumination system which can produce high-contrast images of the targets could be used in the same way. The user-given parameters need to be adjusted according to the grippers of the system, the fibers being studied and the measurements that have to be taken. Although there are many descriptions of measurements of the 2D profile of fibrous objects in the literature, as discussed in Section 2.4.2, no measurements for fiber manipulation have been done before.

The algorithms for the 3D reconstruction of the fibers and their bonds are equally well applicable to any type of fiber or any bond consisting of two fibers. The parameters such as step size for curvature calculation and the width of the smoothing window need to be tuned based on the average straightness and length of the fibers. The parameters of the grasp point detection algorithm need to be tuned for the grippers of the system and the measurements that need to be done. Much research has been conducted on automated microrobotic grasping of 3D objects, but the 3D reconstruction of the objects to be grasped is rare. In fact, automated micro manipulation of fibrous objects (or the rules for it) have never been presented in the literature before.

5.2 Answering the Research Questions

Here, the research questions defined in Section 1.2 are represented along with the answers to these questions as deduced from this thesis.

- Can the imaging of paper fibers and paper fiber bonds be improved to such a level that they can be detected and defined individually with minimal computation, thus enabling the possibility of their efficient automated manipulation?

The developed illumination system exploits the polarizing properties of the fibers in order to produce high-contrast images which can then be segmented efficiently using thresholding. Even global thresholding gives satisfactory results as seen in Publications I and II but the iterative procedure utilized in Publications IV and V is recommended. The novel design of the illumination system enables the use of polarized light in a moving and rotating substrate, thus enabling its use in demanding microrobotic manipulation.

- What information should be gathered from the images of thin, curly and irregular planar objects that wet paper fibers are that would enable the possibility of their automated microrobotic manipulation?

The curvature and the cumulative length of the fibers were found to be the most important facts required for manipulation of planar fibrous objects. The centerline approximation produced with morphological thinning is an efficient approach to obtaining that information. The morphological features of the fibers are well-preserved in the centerline approximation, and other inspections such as detection of overlapping fibers can also be easily performed using this technique. Also, searching for the grasp points is straightforward and involves forming point pairs from the fiber ends and testing different rules on the point pairs.

- How can a microrobotic platform, consisting of the microscope cameras and microgripper actuators required for image-based 3D measurements and grasping experiments, be accurately calibrated?

True 3D point – image point calibration was performed for the 3D measurements and experiments instead of the conventional planar microscope camera calibration often used in the literature and in state-of-the-art micromanipulation systems. The point correspondences were obtained by utilizing the micromanipulators of the microrobotic platform. Planar dot grid patterns were fabricated by exposing photographic paper under a photolithography mask. These were attached to the grippers to facilitate tracking the micromanipulators in the images. The camera matrices needed for the 3D measurements are calculated by linking the pattern location in the image and the micromanipulator position given by the position sensor. The offset between the gripper tip and the pattern is calculated by image-based measurements performed after attaching the patterns.

- How to perform 3D measurements on the thin, curly, highly heterogenous non-planar objects which dry paper fibers are, in order to gain enough information about their depth to enable their automated manipulation?

Using two camera views at a slight angle to each other and utilizing the curvature representation of the skeleton of the target fiber was an efficient approach to forming a 3D approximation of the fiber's centerline. The curvature is a 1D signal and the points where the sign of the curvature changes are detected in the curvature representation as minima and maxima. Corresponding minima and maxima were linked to each other by utilizing filtering and cross-correlation of the curvature signals. The skeleton of a fiber bond needs to be divided into two fibers before using the algorithm. The camera matrices needed for 3D reconstruction were obtained using the calibration procedure described above. The

required image point – 3D point correspondences were obtained by moving the micromanipulator in the cameras' fields of view, tracking the pattern on the manipulator and reading the position sensors of the micromanipulator. This kind of 3D measurement on a micro-robotic platform has seldom been reported in the literature since the parts to be manipulated with state-of-the-art systems usually have known dimensions.

- Is it possible to define suitable grasp points for these thin, curly and irregular objects so that they can be grasped and manipulated by microgripper actuators in an automated manner?

The rules were formed for the valid grasp point pairs on 2D skeletons representing the wet fibers and a combination of three grasp points on 3D skeletons representing the dry fiber bonds. The 2D grasp point pair rules can also be used with the 3D skeletons describing the dry fibers by utilizing only their XY coordinates. The rules for the Z coordinates can be added if needed. The straightness of the fiber section to be grasped with the microgripper is essential for a successful grasp. Also, the grasp point should not be too close to the end of the fiber to ensure a firm grip. The length of the fiber section between the grippers or the distance of the grasp points from the center of the fiber bond are also important for the measurements which have to be done after grasping. These grasping rules have been validated by comparing them to the performance of a human operator and by performing real grasping tests. The rules for automated microrobotic grasping of thin, curly and irregular objects such as natural fibers, or experiments on automated micro-robotic grasping of natural fibers have never been reported in the literature before.

5.3 Discussion and Future Work

In presenting the fundamental principles of automated microrobotic fiber handling, this thesis has shown that although it can be done, there are still many problems to be solved. The most pressing task at the moment is to find the optimal grasping parameters for different types of paper fibers and paper fiber bonds. The parameters suggested in the thesis were experimentally found to be functional, but their reliability could still be improved by fine-tuning. There is a great variety in the dimensions and other physical properties of different fibers and this has to be considered in grasp point detection. Furthermore, a great number of grasping tests have to be performed to validate the parameters.

This thesis discussed the steps needed for the automated grasping of fibers and fiber bonds. The additional steps required for the actual measurements of the physical properties were beyond the scope of the thesis and have to be solved separately for each measurement task. This means, for example, straightening the fiber, pushing it towards the force sensor and reading the force and the deformation of the fiber for the flexibility measurement. It also involves integrating a force sensor into one of the grippers and then processing that reading to measure the bond strength. In addition, to build a fully-automated paper fiber analysis platform requires technologies for feeding the fibers and bonds on to the sample stage, cleaning any possibly attached fibers and debris from the gripper tips and removing the measured fibers and any ungraspable fibers from the sample stage. Suitable methods for fault diagnostics also need to be developed.

References

Ackermann, C., Gottsching, L. & Pakarinen, H. 2009. Papermaking potential of recycled fibre. In: Höke, U. & Schabel, S. (ed.), Recycled fibre and deinking, 2nd ed., Paperi ja puu oy, Helsinki, Finland, pp. 434-515.

Adel, G., Faten, F. & Radhia, A. 2011. Assessing cotton fiber maturity and fineness by image analysis. Journal of Engineered Fibers and Fabrics 6, 2, pp. 50-60.

Ammi, M., Frémont, V. & Ferreira, A. 2009. Automatic camera-based microscope calibration for a telemicromanipulation system using a virtual pattern. IEEE Transactions on Robotics 25, 1, pp. 184-191.

Aronsson, M. 2002. Estimating fibre twist and aspect ratios in 3D voxel volumes. Proceedings of International Conference on Pattern Recognition (ICPR 2002), Quebec, QC, Canada, pp. 218-221.

Axelsson, M. 2006. 3D tracking of cellulose fibres in volume images. Proceedings of International Conference on Image Processing (ICIP 2006), Atlanta, GA, USA, pp. IV309-IV312.

Banerjee, A.G. & Gupta, S.K. 2013. Research in automated planning and control for micromanipulation. IEEE Transactions on Automation Science and Engineering 10, 3, pp. 485-495.

Bartenwerfer, M., Eichhorn, V., Fatikow, S., Becker, M., Savenko, A., Yildiz, I. & Bøggild, P. 2013. Design of a micro-cartridge system for the robotic assembly of exchangeable AFM-probe tips. Proceedings of IEEE/RAS International Conference on Robotics and Automation (ICRA 2013), Karlsruhe, Germany, pp. 1730-1735.

Bert, J., Dembélé, S. & Le Fort-Piat, N. 2007. Performing weak calibration at the microscale, application to micromanipulation. Proceedings of IEEE/RAS International Conference on Robotics and Automation (ICRA 2007), Rome, Italy, pp. 4937-4942.

Besl, P.J. & McKay, N.D. 1992. A method for registration of 3-D shapes, IEEE Transactions on Pattern Analysis and Machine Intelligence, Vol. 14, 2, pp. 239-256.

Biermann, C.J. 1996. Handbook of pulping and papermaking, 2nd ed., Academic Press, San Diego, CA, USA.

Bilen, H., Hocaoglu, M.A., Unel, M. & Sabanovic, A. 2012. Developing robust vision modules for microsystems applications. Machine Vision and Applications 23, 1, pp. 25-42.

Bilen, H. & Unel, M. 2008. Micromanipulation using a microassembly workstation with vision and force sensing. Lecture Notes in Computer Science (including subseries Lecture Notes in Artificial Intelligence and Lecture Notes in Bioinformatics) 5226, pp. 1164-1172.

Bolopion, A., Ni, Z., Agnus, J., Benosman, R. & Regnier, S. 2012. Stable haptic feedback based on a dynamic vision sensor for microrobotics. Proceedings of IEEE/RSJ International Conference on Intelligent Robots and Systems (IROS 2012), Vilamoura, Portugal, pp. 3203-3208.

Bouguet, J.-Y. Camera calibration toolbox for Matlab [accessed 01/2017]. Available: http://www.vision.caltech.edu/bouguetj/calib_doc/index.html.

Bradski, G. & Kaehler, A. 2008. Learning OpenCV: Computer vision with the OpenCV library, O'Reilly Media, CA, USA.

Byun, J.-E. & Nagata, T. 1996. Determining the 3-D pose of a flexible object by stereo matching of curvature representations. Pattern Recognition 29, 8, pp. 1297-1307.

Cappelleri, D.J., Fu, Z. & Fatovic, M. 2012. Caging for 2D and 3D micromanipulation. Journal of Micro-Nano Mechatronics 7, 4, pp. 115-129.

Chinga-Carrasco, G., Kauko, H., Myllys, M., Timonen, J., Wang, B., Zhou, M. & Fossum, J.O. 2008. New advances in the 3D characterization of mineral coating layers on paper. Journal of Microscopy 232, 2, pp. 212-224.

Coeurjolly, D. & Svensson, S. 2003. Estimation of curvature along curves with application to fibres in 3D images of paper. Proceedings of Scandinavian Conference on Image Analysis (SCIA 2003), Halmstad, Sweden, pp. 247-254.

Comin, C.H., Xu, X., Wang, Y., Fontoura Costa, L. da & Yang, Z. 2014. An image processing approach to analyze morphological features of microscopic images of muscle fibers. Computerized Medical Imaging and Graphics 38, 8, pp. 803-814.

Das, A.N., Murthy, R., Popa, D.O. & Stephanou, H.E. 2012. A multiscale assembly and packaging system for manufacturing of complex micro-nano devices. IEEE Transactions on Automation Science and Engineering 9, 1, pp. 160-170.

Eckhart, R., Donoser, M. & Bauer, W. 2009. Single fibre flexibility measurement in a flow cell based device. Proceedings of Pulp and Paper Fundamental Research Symposium: (FRC 2009), Oxford, UK, pp. 247-271.

Edwards, P.J., King, A.P., Maurer Jr., C.R., De Cunha, D.A., Hawkes, D.J., Hill, D.L.G., Gaston, R.P., Fenlon, M.R., Jusczyzck, A., Strong, A.J., Chandler, C.L. & Gleeson, M.J. 2000. Design and evaluation of a system for microscope-assisted guided interventions (MAGI). IEEE Transactions on Medical Imaging 19, 11, pp. 1082-1093.

Eichhorn, V., Carlson, K., Andersen, K.N., Fatikow, S. & Bøggild, P. 2007. Nanorobotic manipulation setup for pick-and-place handling and nondestructive characterization of carbon nanotubes. Proceedings of IEEE/RSJ International Conference on Intelligent Robots and Systems (IROS 2007), San Diego, CA, USA, pp. 291-296.

Essen, M. von, Hirvonen, J., Kuikka, S. & Kallio, P. 2014. Robotic software frameworks and software component models in the development of automated handling of individual natural fibers. Journal of Micro-Bio Robotics 9, 1-2, pp. 29-45.

Estaña, R., Seyfried, J., Schmoeckel, F., Thiel, M., Buerkle, A. & Woern, H. 2004. Exploring the micro- and nanoworld with cubic centimetre-sized autonomous microrobots. Industrial Robot 31, 2, pp. 159-178.

Fatikow, S., Eichhorn, V., Wich, T., Sievers, T., Hanssler, O. & Andersen, K.N. 2007. Depth-detection methods for CNT manipulation and characterization in a scanning electron microscope. Proceedings of IEEE International Conference on Mechatronics and Automation (ICMA 2007), Harbin, China, pp. 45-50.

Fischer, W.J., Hirn, U., Bauer, W. & Schennach, R. 2012. Testing of individual fiber-fiber joints under biaxial load and simultaneous analysis of deformation. Nordic Pulp and Paper Research Journal 27, 2, pp. 237-244.

Fluid Imaging Technologies Inc. 2012. Fiber analysis using FlowCAM. FlowCAM Application Note #111 .

Guo, Z. & Hall, R.W. 1989. Parallel thinning with two-subiteration algorithms. Communications of the ACM 32, 3, pp. 359-373.

Gustafsson, J., Alén, R., Engström, J., Korpinen, R., Kuusisto, P., Leavitt, A., Olsson, K., Piira, J., Samuelsson, A. & Sundquist, J. 2011. Pulping. In: Fardim, P. (ed.), Chemical pulping part 1, fibre chemistry and technology, 2nd ed., Paperi ja puu oy, Helsinki, Finland, pp. 190-381.

Hamad, W.Y. & Provan, J.W. 1995. Microstructural cumulative material degradation and fatigue-failure micromechanisms in wood-pulp fibres. Cellulose 2, 3, pp. 159-177.

Hartley, R. & Zisserman, A. 2004. Multiple View Geometry in Computer Vision. Cambridge University Press, West Nyack, NY, USA.

Heikkilä, J. & Silven, O. 1997. Four-step camera calibration procedure with implicit image correction. Proceedings of IEEE Conference on Computer Vision and Pattern Recognition (CVPR 1997), San Juan, Puerto Rico, pp. 1106-1112.

Heikkurinen, A. 1999. Single fiber properties. In: Levlin, J. & Söderhjelm, L. (ed.), Pulp and paper testing, Paperi ja puu oy, Helsinki, Finland, pp. 19-38.

Helle, T. 1978. How forming fabric design affects drainage and release. Pulp and Paper Magazine of Canada 79, 11, pp. 91-98.

Hirn, U. & Bauer, W. 2006. Review of image analysis based methods to evaluate fiber properties. Lenzinger Berichte 86, 1, pp. 96-105.

Hirn, U. & Schennach, R. 2015. Comprehensive analysis of individual pulp fiber bonds quantifies the mechanisms of fiber bonding in paper. Scientific Reports 5, 10503, pp. 1-9.

Hirvonen, J., Ronkanen, P., Ylikomi, P., Blauer, M., Suuronen, R., Skottman, H. & Kallio, P. 2008. Microcutting of living tissue slices and stem cell colonies by using mechanical tool and liquid jet. IEEE International Conference on Biomedical Robotics and Biomechatronics (BioRob 2008), pp. 612-617.

Hou, B.-P., Li, P. & Song, Z.-H. 2005. Measurement of the characteristics of pulp fibers based on computer vision. Zhongguo Zaozhi Xuebao/Transactions of China Pulp and Paper 20, 1, pp. 190-195.

Ikiz, Y., Rust, J.P., Jasper, W.J. & Trussell, H.J. 2001. Fiber length measurement by image processing. Textile Research Journal 71, 10, pp. 905-910.

Inkilä, K. 2005. Homogeneous least squares problem. Photogrammetric Journal of Finland 19, 2, pp. 34-42.

Jasper, D., Diederichs, C., Stolle, C. & Fatikow, S. 2011. Automated robot-based separation and palletizing of microcomponents. IEEE International Symposium on Assembly and Manufacturing (ISAM 2011), pp. 1-6.

Jayne, B.A. 1959. Mechanical properties of wood fibres. TAPPI Journal 42, pp. 461-467.

Kannala, J., Heikkilä, J. & Brandt, S.S. 2009. Geometric camera calibration. In: Bah, B.W. (ed.), Wiley Encyclopedia of Computer Science and Engineering, John Wiley & Sons, Inc., Hoboken, NJ, USA.

Kappel, L., Hirn, U., Gilli, E., Bauer, W. & Schennach, R. 2010a. Revisiting polarized light microscopy for fiber-fiber bond area measurement - Part I: Theoretical fundamentals. Nordic Pulp and Paper Research Journal 25, 1, pp. 65-70.

Kappel, L., Hirn, U., Gilli, E., Bauer, W. & Schennach, R. 2010b. Revisiting polarized light microscopy for fiber-fiber bond area measurement - Part II: Proving the applicability. Nordic Pulp and Paper Research Journal 25, 1, pp. 71-75.

Karlsson, H. 2010. Strength properties of paper produced from softwood kraft pulp. PhD thesis, Karlstad University, Karldstad, Sweden, p. 11.

Kawaji, A., Arai, F. & Fukuda, T. 2001. 3D calibration for micro-manipulation with precise position measurement. Journal of Micromechatronics 1, 2, pp. 117-130.

Kim, K., Liu, X., Zhang, Y. & Sun, Y. 2008. Micronewton force-controlled manipulation of biomaterials using a monolithic MEMS microgripper with two-axis force feedback. Proceedings of IEEE/RAS International Conference on Robotics and Automation (ICRA 2008), Pasadena, CA, USA, pp. 3100-3105.

Komati, B., Rabenorosoa, K., Clevy, C. & Lutz, P. 2013. Automated guiding task of a flexible micropart using a two-sensing-finger microgripper. IEEE Transactions on Automation Science and Engineering 10, 3, pp. 515-524.

Kovanen, K., Lukkari, M., Purmonen, S., Ylikomi, T., Viitanen, J. & Kallio, P.J. 2007. Electric impedance assisted micropipette aspiration. Proceedings of IEEE Annual International Conference on Engineering in Medicine and Biology (EMBC 2007), Lyon, France, pp. 5822-5825.

Kulachenko, A., Gradin, P. & Koivurova, H. 2007. Modelling the dynamical behaviour of a paper web. Part I & Part II. Computers & Structures 85, 3-4, pp. 131-157.

Kulachenko, A. & Uesaka, T. 2012. Direct simulations of fiber network deformation and failure. Mechanics of Materials 51, pp. 1-14.

Kwon, N., Pyo, J., Lee, S.-J. & Je, J.H. 2013. 3-D worm tracker for freely moving C. elegans. PLoS ONE 8, 2, pp. 1-6.

Lam, L., Lee, S. & Suen, C.Y. 1992. Thinning methodologies – A comprehensive survey. IEEE Transactions on Pattern Analysis and Machine Intelligence 14, 9, pp. 869-885.

Latifi, S.K., Saketi, P. & Kallio, P. 2015. Microrobotic system for multi-rate measurement of bio-based fibres Z-directional bond strength. Journal of Micro-Bio Robotics 10, 1, pp. 13-26.

Leopold, B. & McIntosh, D.C. 1961. Chemical composition and physical properties of wood fibres: III. Tensile strength of individual fibres from alkali extracted loblolly pine holocellulose. TAPPI Journal 44, 3, pp. 235-240.

Lindholm, C., Jäkärä, J., Persson, M. & Mårtens, H. 2009. Bleaching of mechanical pulps. In: Lönnberg, B. (ed.), Mechanical pulping, 2nd ed., Paperi ja puu oy, Helsinki, Finland, pp. 360-398.

Lindström, T., Wågberg, L. & Larsson, T. 2005. On the nature of joint strength in paper – a review of dry and wet strength resins used in paper manufacturing. Proceedings of Pulp and Paper Fundamental Research Symposium (FRC 2005), Cambridge, UK, pp. 457-562.

Lorbach, C., Fischer, W.J., Gregorova, A., Hirn, U. & Bauer, W. 2014. Pulp fiber bending stiffness in wet and dry state measured from moment of inertia and modulus of elasticity. Bioresources 9, 3, pp. 5511-2228.

Lowe, R.M. 2007. The deformation behavior of wet lignocellulosic fibers. PhD thesis, Georgia Institute of Technology, Atlanta, GA, USA.

Magnusson, M.S. & Östlund, S. 2011. Inter-fibre bond strength and combined normal and shear loading. Proceedings of Progress in Paper Physics Seminar (PPPS 2011), Graz, Austria, pp. 205-207.

Matsuoka, H., Komazaki, T., Mukai, Y., Shibusawa, M., Akane, H., Chaki, A., Uetake, N. & Saito, M. 2005. High throughput easy microinjection with a single-cell manipulation supporting robot. Journal of Biotechnology 116, 2, pp. 185-194.

Mayhood, C.H., Kallmes, J.O.J. & Cauley, M.M. 1962. Mechanical properties of paper; part ii: Measured shear strength of individual fiber to fiber contacts. TAPPI Journal 45, 1, pp. 69-73.

McDonald, J.C. & Whitesides, G.M. 2002. Poly(dimethylsiloxane) as a material for fabricating microfluidic devices. Accounts of Chemical Research 35, 7, pp. 491-499.

Meindersma, E., Robertson, A.A. & Mason, S.G. 1961. The measurement of fiber flexibility. Pulp and Paper Magazine of Canada 62, 1, pp. T3-T10.

Mikczinski, M., Nguyen, H.X. & Fatikow, S. 2013. Assessing transverse fibre properties: compression and artificial hornification by periodic compression. Proceedings of Pulp and Paper Fundamental Research Symposium (FRC 2013), Cambridge, UK, pp. 803-820.

Moons, T., Van Gool, L. & Vergauwen, M. 2009. 3D Reconstruction from multiple images part 1: Principles. Foundations and Trends in Computer Graphics and Vision 4, 4, pp. 287-398,

Mott, L. 1995. Micro mechanical properties and fracture mechanisms of single wood fibers. PhD thesis, University of Michigan, Ann Arbor, MI, USA.

Niemistö, A., Dunmire, V., Yli-Harja, O., Zhang, W. & Shmulevich, I. 2005. Robust quantification of in vitro angiogenesis through image analysis. IEEE Transactions on Medical Imaging 24, 4, pp. 549-553.

Oliphant, T.E. 2007. Python for scientific computing. Computing in Science & Engineering 9, 3, pp. 10-20.

Olson, J.A., Kuhn, D.C.S., Lu, X. & Robertson, A.G. 1995. A dynamic wet fibre flexibility device. Journal of Pulp and Paper Science 21, 10, pp. J337-J342.

Paavilainen, L. 1993. Conformability – flexibility and collapsibility – of sulphate pulp fibres. Paperi & Puu 75, 9, pp. 689-702.

Page, D.H., El Hosseiny, F., Winkler, K. & Lancaster, A.P.S. 1977. Elastic modulus of single wood pulp fibers. TAPPI Journal 60, pp. 114-117.

Pawashe, C. & Sitti, M. 2006. Two-dimensional vision-based autonomous microparticle manipulation using a nanoprobe. Journal of Micromechatronics 3, 3, pp. 285-306.

Probst, M., Hürzeler, C., Borer, R. & Nelson, B.J. 2009. A microassembly system for the flexible assembly of hybrid robotic mems devices. International Journal of Optomechatronics 3, 2, pp. 69-90.

Ritter, M., Hemmleb, M., Sinram, O., Albertz, J. & Hohenbert, H. 2004. A versatile 3D calibration object for various micro-range measurements methods. Proceedings of ISPRS Congress (ISPRS 2004), Istanbul, Turkey, pp. 696-702.

Rusu, M., Mörseburg, K., Gregersen, Ø., Yamakawa, A. & Liukkonen, S. 2011. Fibre flexibility of TMP. BioResources 6, 1, pp. 641-655.

Saeed, K., Tabędzki, M., Rybnik, M. & Adamski, M. 2010. K3M: A universal algorithm for image skeletonization and a review of thinning techniques. International Journal of Applied Mathematics and Computer Science 20, 2, pp. 317-335.

Saketi, P. 2015. Microrobotic platform with integrated force sensing microgrippers for characterization of fibrous materials: Case study on individual paper fibers. PhD Thesis, Tampere University of Technology, Tampere, Finland.

Saketi, P. & Kallio, P. 2011a. Measuring bond strenghts of individual paper fibers using microrobotics. Proceedings of Progress in Paper Physics Seminar (PPPS 2011), Graz, Austria, pp. 199-202.

Saketi, P., Latifi, S.K. & Kallio, P. 2014. Microrobotic platform for the measurement of fiber-fiber friction. Proceedings of Progress in Paper Physics Seminar (PPPS 2014), Raleigh, NC, USA, pp. 1-4.

Saketi, P. & Kallio, P. 2011b. Microrobotic platform for making, manipulating and breaking individual paper fiber bonds. Proceedings of IEEE International Symposium on Assembly and Manufacturing (ISAM 2011), Tampere, Finland, pp. 1-6.

Saketi, P., Wangyang, P., Li, H., Wang, Q. & Kallio, P. 2015a. Electroplated nickel microspring and low-friction precision linear slider: A novel micro-force sensing tool. Proceedings of IEEE/RAS International Conference on Robotics and Automation (ICRA 2015), Seattle, WA, USA, pp. 2679-2684.

Saketi, P., Treimanis, A., Fardim, P., Ronkanen, P. & Kallio, P. 2010. Microrobotic platform for manipulation and flexibility measurement of individual paper fibers. Proceedings of IEEE/RSJ International Conference on Intelligent Robots and Systems (IROS 2010), Taipei, Taiwan, pp. 5762-5767.

Saketi, P., Essen, M. von, Mikczinski, M., Heinemann, S., Fatikow, S. & Kallio, P. 2012. A flexible microrobotic platform for handling microscale specimens of fibrous materials for microscopic studies. Journal of microscopy 248, 2, pp. 163-171.

Saketi, P., Latifi, S.K., Hirvonen, J., Rajala, S., Vehkaoja, A., Salpavaara, T., Lekkala, J. & Kallio, P. 2015b. PVDF microforce sensor for the measurement of Z-directional strength in paper fiber bonds. Sensors and Actuators A: Physical 222, 1, pp. 194-203.

Salvi, J., Armangué, X. & Batlle, J. 2002. A comparative review of camera calibrating methods with accuracy evaluation. Pattern Recognition 35, 7, pp. 1617-1635.

Savia, M. & Koivo, H.N. 2009. Contact micromanipulation – Survey of strategies. IEEE/ASME Transactions on Mechatronics 14, 4, pp. 504-514.

Schniewind, A.P., Ifju, G. & Brink, D.L. 1966. Effect of drying on the flexural rigidity of single fibres. In: Bolam, F. (ed.), Consolidation of the Paper Web, Volume 1, Technical Section of the British Paper and Board Makers' Association, London, UK, pp. 538-543.

Schniewind, A.P., Nemeth, L.J. & Brink, D.L. 1964. Fiber and pulp properties I. Shear strength of single fiber crossings. TAPPI Journal 47, 4, pp. 244.

Seth, R.S. 2001. The difference between never-dried and dried chemical pulps. Proceedings of TAPPI Pulping Conference, Seattle, WA, USA, pp. 289-304.

Shin, E.H., Cho, K.S., Seo, M.H. & Kim, H. 2008. Determination of electrospun fiber diameter distributions using image analysis processing. Macromolecular Research 16, 4, pp. 314-319.

Sirviö, J. 2008. Fibers and bonds. In: Niskanen, K. (ed.), Paper Physics, 2nd ed., Paperi ja puu oy, Helsinki, Finland, pp. 60-92.

Sitti, M. & Hashimoto, H. 1999. Two-dimensional fine particle positioning using a piezoresistive cantilever as a micro/nano-manipulator. Proceedings of IEEE/RAS International Conference on Robotics and Automation (ICRA 1999), Detroit, MI, USA, pp. 2729-2735 vol.4.

Stratton, R.A. & Colson, N.L. 1990. Dependence of fiber/fiber bonding on some papermaking variables. Atlanta, GA, USA, Institute of Paper Science and Technology. IPST Technical Paper Series.

Sun, Y., Nelson, B.J. & Greminger, M.A. 2005. Investigating protein structure change in the zona pellucida with a microrobotic system. International Journal of Robotics Research 24, 2-3, pp. 211-218.

Sundholm, J. & Lönnberg, B. 2009. Idea of mechanical pulping. In: Lönnberg, B. (ed.), Mechanical pulping, 2nd ed., Paperi ja puu oy, Helsinki, Finland, pp. 18-22.

Sutherland, I.E. 1974. Three-dimensional data input by tablet. Proceedings of the IEEE 62, 4, pp. 453-461.

Tam Doo, P.A. & Kerekes, R.J. 1981. Method to measure wet fiber flexibility. TAPPI Journal 64, 3, pp. 113-116.

Tamadazte, B., Dembele, S. & Le Fort-Piat, N. 2008. A multiscale calibration of a photon video microscope for visual servo control: Application to micromanipulation. Proceedings of IEEE International Workshop on Robotic and Sensors Environments (ROSE 2008), Ottawa, ON, Canada, pp. 29-34.

Tamadazte, B., Marchand, E., Dembélé, S. & Le Fort-Piat, N. 2010. CAD model-based tracking and 3D visual-based control for MEMS microassembly. International Journal of Robotics Research 29, 11, pp. 1416-1434.

Tanikawa, T. & Arai, T. 1999. Development of a micro-manipulation system having a two-fingered micro-hand. IEEE Transactions on Robotics and Automation 15, 1, pp. 152-162.

TAPPI Quality and Standards Department 2002. Forming handsheets for physical tests of pulp. GA, USA, The Technological Association of Paper and Pulp Industry (TAPPI). T-205 sp-02.

TAPPI Quality and Standards Department 2001. Physical testing of pulp handsheets. GA, USA, The Technological Association of the Pulp and Paper Industry (TAPPI). T-220.

Torgnysdotter, A., Kulachenko, A., Gradin, P. & Wågberg, L. 2007. Fiber/fiber crosses: Finite element modeling and comparison with experiment. Journal of Composite Materials 41, 13, pp. 1603-1618.

Tsai, R.Y. 1987. A Versatile camera calibration technique for high-accuracy 3D machine vision metrology using off-the-shelf TV cameras and lenses. IEEE Journal of Robotics and Automation 3, 4, pp. 323-344.

Wang, W., Liu, X., Gelinas, D., Ciruna, B. & Sun, Y. 2007. A fully automated robotic system for microinjection of zebrafish embryos. PLoS ONE 2, 9, pp. e862-1-e862-9.

Wang, X. 2006. Improving the papermaking properites of kraft pulp by controlling hornification and internal fibrillation. PhD Thesis, Helsinki University of Technology, Helsinki, Finland.

Wang, H., Mao, C., Sari-Sarraf, H. & Hequet, E.F. 2008. Accurate length measurement of multiple cotton fibers. Journal of Electronic Imaging 17, 3, pp. 031110-1-031110-10.

Wang, L., Ren, L., Mills, J.K. & Cleghorn, W.L. 2010. Automated 3-D micrograsping tasks performed by vision-based control. IEEE Transactions on Automation Science and Engineering 7, 3, pp. 417-426.

Wason, J.D., Wen, J.T., Gorman, J.J. & Dagalakis, N.G. 2012. Automated multiprobe microassembly using vision feedback. IEEE Transactions on Robotics 28, 5, pp. 1090-1103.

Willför, S., Alén, R., Dam, J. van, Liu, Z. & Tähtinen, M. 2011. Raw materials. In: Fardim, P. (ed.), Chemical pulping part 1, fibre chemistry and technology, 2nd ed., Paperi ja puu oy, Helsinki, Finland, pp. 16-186.

Xie, H. & Régnier, S. 2009. Three-dimensional automated micromanipulation using a nanotip gripper with multi-feedback. Journal of Micromechanics and Microengineering 19, 7, pp.1-9.

Xing, D., Xu, D. & Li, H. 2014. A sequence of micro-assembly for irregular objects based on a multiple manipulator platform. Proceedings of IEEE/RSJ International Conference on Intelligent Robots and Systems (IROS 2014), Chicago, IL, USA, pp. 761-766.

Ye, C., Sundstrom, M.O. & Remes, K. 1994. Microscopic transmission ellipsometry: measurement of the fibril angle and the relative phase retardation of single, intact wood pulp fibers. Applied Optics 33, 28, pp. 6626-6637.

Zakharov, A.A., Tuzhilkin, A.Y. & Zhiznyakov, A.L. 2015. Finding correspondences between Images using descriptors and graphs. Procedia Engineering, 129, pp. 391-396.

Zhang, Z. 2000. A flexible new technique for camera calibration. IEEE Transactions on Pattern Analysis and Machine Intelligence 22, 11, pp. 1330-1334.

Zhang, Z. 2004. Camera calibration. In: Medioni, G. & Kang, S.B. (ed.), Emerging Topics in Computer Vision, 1st ed., Prentice Hall, NJ, USA, pp. 5-43.

Zhou, Q., Korhonen, P., Laitinen, J. & Sjövall, S. 2006. Automatic dextrous microhandling based on a 6-DOF microgripper. Journal of Micromechatronics 3, 3, pp. 359-387.

Zhou, Y. & Nelson, B.J. 1999. Calibration of a parametric model of an optical microscope. Optical Engineering 38, 12, pp. 1989-1995.

Tampereen teknillinen yliopisto
PL 527
33101 Tampere

Tampere University of Technology
P.O.B. 527
FI-33101 Tampere, Finland

ISBN 978-952-15-3904-6
ISSN 1459-2045